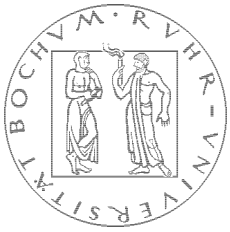

Ruhr University Bochum
Lehrstuhl für Technische Mechanik

Preprint 04-2005

On advanced solution strategies to overcome locking effects in strong discontinuity approaches

J. Mosler

This is a preprint of an article published in:

International Journal for Numerical Methods in Engineering, Vol. 63, 1373–1401, (2005)

On advanced solution strategies to overcome locking effects in strong discontinuity approaches

J. Mosler *

Institute of Mechanics, Ruhr University Bochum
Universitätsstr. 150,D-44780 Bochum, Germany
E-Mail: mosler@tm.bi.ruhr-uni-bochum.de
URL: www.tm.bi.ruhr-uni-bochum.de/mosler

SUMMARY

This paper is concerned with the analysis of locking effects resulting from different orientations of micro-defects and those of the corresponding macro-defects. Based on a mixed-mode material model embedded within the framework of the strong discontinuity approach (SDA), the described locking effect is illustrated by means of a crack analysis of a notched concrete beam. To overcome the deficiency of the proposed finite element model, the original SDA is modified and extended. For that purpose, two different advanced numerical formulations are developed: a rotating crack approach and a multiple crack approach. Restricting the governing equations to the material point level, a standard return-mapping procedure is applied to the algorithmic formulations of both models. The applicability and the performance of the proposed numerical implementations are investigated by means of a re-analysis of the two-dimensional notched concrete beam.

1 INTRODUCTION

Numerical analyses of material failure represent an important tool for the safety estimation of engineering structures. However, despite considerable progress made in computational failure mechanics, many questions are still unanswered and controversially discussed in the scientific community. One of these problems is concerned with the modeling of strain localization phenomena.

From the mathematical point of view, initiation of strain localization results in the loss of ellipticity of the governing equations [1, 2]. The partial differential equation changes from the elliptic to the hyperbolic type (in the static case). As a consequence, the considered problem becomes ill-posed and its solution is not unique and depends strongly on the width of the zone showing localized deformations. In the limiting case (the width of this zone converges to zero), material failure without any dissipation appears. Clearly, this represents an unphysical solution. Applying the finite element method to the analysis of material failure, the described implications of strain localization result in a lack of invariance of the numerically computed solutions with respect to the spatial discretization (see [3, 4]).

To overcome the mentioned deficiencies of classical (local) continuum models, various enhanced models, such as nonlocal or gradient-enhanced models and COSSERAT continua, have

*Contract/grant sponsor: Deutsche Forschungsgemeinschaft (DFG) through the project A4 under supervision of Prof. O.T. Bruhns within the Collaborative Research Centre 398

been proposed in the last decade, cf. [5–10]. However, despite the objectivity of the solutions obtained numerically from these models, they are less suitable for large-scale applications. Since these approaches require a sufficiently fine resolution of the localization zone to guarantee mesh objectivity (at least two to three elements across the thickness of this zone are required), they result in high computational costs.

In recent years, numerical models based on discontinuous displacement fields such as [11–18] have become very popular for the analysis of material failure. In these concepts, the displacement jumps are associated with the opening of cracks in brittle materials [19–21] or the sliding of shear bands [22–24]. Since the localized deformation is modeled by a surface of discontinuous displacements within the respective finite element, this method allows to use relatively large elements compared to the width of the localization zone. As a consequence, this approach is suitable for large-scale applications. In what follows, models in which the discontinuous displacement field is incorporated by means of an enhanced assumed strain concept (EAS) will be referred to as strong discontinuity approaches (SDA), cf. [14]. These models differ from those formulations which truly model a displacement discontinuity, such as the X-FEM [17, 25].

Assuming inelastic deformations to be restricted to the localization surface, the material response is governed by means of traction-separation laws [13, 14, 21] (instead of classical stress-strain relationships) connecting the traction vector acting on the localization zone with the displacement discontinuity. The surface defined by the points showing displacement jumps is most frequently interpreted as a material surface and consequently, kept fixed [13–15, 19]. If macro-defects such as fully open cracks are considered, a fixed localization surface is indeed physical. However, the traction-separation law is often also applied to the modeling of micro-defects such as micro-cracks [19, 20, 26]. Consequently, the orientation of the localization surface is computed based on the micro-defects and not on the macro-defects (the micro-defects form earlier than the macro-defects). However, these micro-defects may close while additional micro-cracks may start opening. Consequently, the direction of the macro-crack differs from that of the computed localizations surface. This may lead to locking effects as reported in [16, 19].

To overcome the described locking effect, different advanced solution strategies have been proposed [19, 27]. In [19], the strong discontinuity approach has been coupled with a nonlocal damage model while in [27], an extended finite element model (X-FEM) has been enhanced using a viscoplastic regularization. Both models capture the micro-defects by means of a continuous model (nonlocal damage theory or viscoplasticity). If a specific threshold is reached, a transition from the respective continuous model to the discontinuous model is applied. However, the considered continuous models require a sufficient fine resolution of the localization zone to guarantee mesh objectivity. Hence, both models result in high computational costs and consequently, they are less suitable for large-scale applications.

Alternatively, the discontinuous model itself can be modified. In this paper, two different concepts will be proposed. On the one hand, the assumption of a time independent localization surface can be abolished, resulting in the so-called rotating localization formulation, cf. [16, 21]. In contrast to the works just cited, the numerical framework which will be presented in this paper is not restricted to a specific traction-separation law. The suggested finite element model can be applied to any plasticity based interface law as well as to a broad range of different damage type constitutive models.

It is evident that allowing the crack to rotate, crack path continuity cannot be enforced. Consequently, the discontinuous displacement field has to be modeled in an incompatible sense.

As an alternative to overcome the described locking effect, the number of possible localization surfaces within the respective finite element can be increased, resulting in a multiple

localization surface formulation. Considering intersecting failure zones, crack close effects and the formation of new micro-defects with different orientations are modeled in a consistent manner. Analogously to the rotating localization surface formulation, the presented multiple localization surface approach can be applied to any plasticity based interface law as well as to a broad range of different damage type constitutive models.

In this paper, both the rotating as well as the multiple localization surface formulation are investigated. Advantages and disadvantages of both models are analyzed critically.

The paper is organized as follows: Section 2 is concerned with a concise summary of the fundamental kinematic assumptions of the SDA. The development of the constitutive equations is addressed in Section 3. In contrast to previously published works on this topic, the most general plasticity based traction-separation law is considered and subsequently, specialized to an associative mixed-mode material model. Section 4 is concerned with the numerical implementation. In contrast to other models in the literature, the proposed algorithmic formulation holds for any plasticity based traction-separation law. In Section 5, a numerical analysis of a notched concrete beam using a single fixed crack concept in conjunction with the suggested mixed-mode material model demonstrates the described locking effect. To overcome the deficiencies of the suggested numerical model, two advanced approaches are developed. Section 6 deals with the rotating crack model while the respective formulation of a multiple crack model is given in Section 7. A numerical re-analysis of the notched concrete beam illustrates the applicability as well as the performance of both approaches.

2 KINEMATICS: DISCONTINUOUS DEFORMATION MAPPINGS

This section contains a short summary of discontinuous deformation mappings. Starting with a general framework, we focus on the kinematics of the strong discontinuity approach (SDA) as proposed in [13, 22, 28–30].

In what follows, $\Omega \subset \mathbb{R}^3$ is an open bounded set and $\boldsymbol{X}_0 \in \Omega$ a (fixed) point. The domain Ω is assumed to be separated by means of a two-dimensional sub manifold $\partial_{\mathrm{s}}\Omega$, see Figure 1. The normal vector field of this hyperplane is denoted as $\boldsymbol{N}$. From a physical point of view, $\partial_{\mathrm{s}}\Omega$ may represent a crack surface occurring in brittle materials or a slip band in ductile metals. Clearly, the cut $\partial_{\mathrm{s}}\Omega$ defines a partition of the body Ω, i.e. $\Omega = \Omega^- \cup \Omega^+ \cup \partial_{\mathrm{s}}\Omega$. Based on this

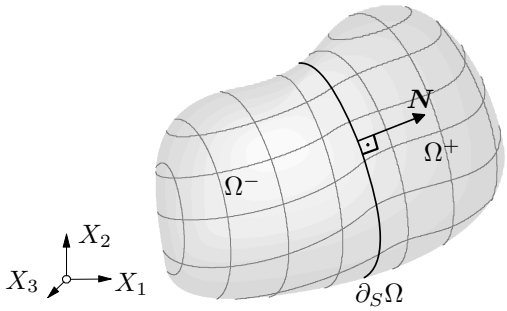

Figure 1: Body $\Omega \subset \mathbb{R}^3$ separated into two parts Ω^- and Ω^+ by a two-dimensional sub manifold $\partial_{\mathrm{s}}\Omega$.

decomposition, a displacement field of the type

$$\boldsymbol{u}(\boldsymbol{X}) = \boldsymbol{u}^-(\boldsymbol{X}) + H_{\mathrm{s}}\, \hat{\boldsymbol{u}}(\boldsymbol{X}), \qquad \forall\, \boldsymbol{X} \in \Omega \tag{1}$$

is adopted, with $\boldsymbol{u}^-, \hat{\boldsymbol{u}} \in \mathcal{C}^\infty(\Omega, \mathbb{R}^3)$ and H_s denoting the Heaviside function. That is, the displacement field is assumed as smooth in $\Omega^\pm := \Omega^+ \cup \Omega^-$, while it may be discontinuous across $\partial_\mathrm{s}\Omega$. These restrictions are reasonable, since in Section 4, an polynomial approximation will be applied to $\boldsymbol{u}|_{\Omega^\pm}$. They allow to introduce the discontinuity of the displacement field $[\![\boldsymbol{u}]\!]$ as

$$[\![\boldsymbol{u}(\boldsymbol{X}_0)]\!] := \boldsymbol{u}^+(\boldsymbol{X}_0) - \boldsymbol{u}^-(\boldsymbol{X}_0) \quad \forall \boldsymbol{X}_0 \in \partial_\mathrm{s}\Omega, \tag{2}$$

by means of the left hand limit $\boldsymbol{u}^-(\boldsymbol{X}_0)$ and the right hand limit $\boldsymbol{u}^+(\boldsymbol{X}_0)$ of the displacement mapping at $\boldsymbol{X}_0 \in \partial_\mathrm{s}\Omega$.

So far, a rather general discontinuous displacement field has been considered. Now, the displacement field (1) is specified to the kinematics of the strong discontinuity approach (SDA). According to SIMO & OLIVER [14, 22], a displacement field of the type

$$\boldsymbol{u} = \bar{\boldsymbol{u}} + [\![\boldsymbol{u}]\!] \ (H_\mathrm{s} - \varphi), \quad \text{with} \quad \bar{\boldsymbol{u}} \in \mathcal{C}^\infty(\Omega, \mathbb{R}^3), \ \varphi \in \mathcal{C}^\infty(\Omega, \mathbb{R}). \tag{3}$$

is assumed. By comparison of Equation (3) with Equation (1), the identities

$$\boldsymbol{u}^- = \bar{\boldsymbol{u}} + [\![\boldsymbol{u}]\!] \ \varphi \quad \text{and} \quad \hat{\boldsymbol{u}} = [\![\boldsymbol{u}]\!]\,. \tag{4}$$

are obtained. Consequently, the kinematics associated with Equation (3) fall into the more general class of models spanned by the displacement mapping (1). The smooth ramp function φ in Equation (3) allows to prescribe the Dirichlet boundary conditions in terms of $\bar{\boldsymbol{u}}$, cf. [14, 22] and Subsection 4.1. From computing the generalized derivative $D(\bullet)$ of the displacement field (3), the linearized strain tensor $\boldsymbol{\varepsilon}$ is obtained as

$$\boldsymbol{\varepsilon} = \boldsymbol{\nabla}^\mathrm{sym}\bar{\boldsymbol{u}} - ([\![\boldsymbol{u}]\!] \otimes \boldsymbol{\nabla}\varphi)^\mathrm{sym} + ([\![\boldsymbol{u}]\!] \otimes \boldsymbol{N})^\mathrm{sym} \ \delta_\mathrm{s} + \boldsymbol{\nabla}^\mathrm{sym}[\![\boldsymbol{u}]\!] \ (H_\mathrm{s} - \varphi)\,, \tag{5}$$

with $\boldsymbol{\nabla}(\bullet) := \partial(\bullet)/\partial\boldsymbol{X}$. In Equation (5), the generalized derivative of the Heaviside function, i.e. $D(H_\mathrm{s}) = \boldsymbol{N}\ \delta_\mathrm{s}$, has been applied. Here and henceforth, δ_s denotes the singularly distributed DIRAC-delta function. It is obvious that Equation (5) has to be interpreted in a distributional sense, cf. [31].

Following SIMO and co-workers [13, 14, 22], the presented finite element formulation is based on the enhanced assumed strain concept (EAS), cf. [32, 33]. That is, only the enhanced strains resulting from the discontinuous displacement field appear explicitly in the proposed model. According to the EAS concept, the enhanced strains are modeled in an incompatible fashion. As a consequence, it is admissible to neglect the gradient of the displacement discontinuity, i.e. $\boldsymbol{\nabla}^\mathrm{sym}[\![\boldsymbol{u}]\!] = \boldsymbol{0}$. Hence, a linearized strain tensor of the type

$$\boldsymbol{\varepsilon} := \boldsymbol{\nabla}^\mathrm{sym}\bar{\boldsymbol{u}} - \underbrace{([\![\boldsymbol{u}]\!] \otimes \boldsymbol{\nabla}\varphi)^\mathrm{sym}}_{:=\,\tilde{\boldsymbol{\varepsilon}}} + ([\![\boldsymbol{u}]\!] \otimes \boldsymbol{N})^\mathrm{sym}\ \delta_\mathrm{s}. \tag{6}$$

is adopted.

Remark 1: The strain tensor (6) represents the symmetric part of the generalized derivative of the displacement field (3) only if $\boldsymbol{\nabla}[\![\boldsymbol{u}]\!] = \boldsymbol{0}$. Hence, the additive decomposition of the strains, according to Equation (6), holds only in an incompatible fashion. However, since an EAS concept is adopted, the strain tensor (6) is suitable and captures the strains resulting from a discontinuous displacement field.

3 CONSTITUTIVE EQUATIONS: TRACTION-SEPARATION LAWS

The kinematics (6) of the SDA are based on two different displacement fields: $\bar{\boldsymbol{u}}$ and $[\![\boldsymbol{u}]\!]$. In this section, the constitutive equations associated with these fields are presented.

According to Section 2, the strains in $\Omega^{\pm}$ are regularly distributed. Consequently, standard stress-strain based continuum models can be applied. Since the main focus of the present paper is on the modeling of localized material failure, HOOKE's law is adopted for points belonging to $\Omega^{\pm}$. That is, the stresses $\boldsymbol{\sigma}$ in $\Omega^{\pm}$ are computed by means of the elastic fourth-order constitutive tensor $\mathbb{C}$ ($\boldsymbol{\sigma} = \mathbb{C} : \boldsymbol{\varepsilon}$). However, it should be emphasized that any classical continuum model, such as plasticity or a damage theory, can be easily applied as well.

In contrast to $\Omega^{\pm}$, the material response in $\partial_{\mathrm{s}}\Omega$ follows from a traction-separation law. Using the compatibility condition at the localization surface, i.e. continuity of the traction vector across $\partial_{\mathrm{s}}\Omega$,

$$\boldsymbol{t}_{\mathrm{s}}(\boldsymbol{X}_0) = \boldsymbol{t}^{+}(\boldsymbol{X}_0), \quad \text{with} \quad \boldsymbol{t} := \boldsymbol{\sigma} \cdot \boldsymbol{N}, \quad \boldsymbol{t}_{\mathrm{s}} := \boldsymbol{t}|_{\partial_{\mathrm{s}}\Omega}, \tag{7}$$

a traction-separation law of the type

$$\boldsymbol{t}^{+} = \boldsymbol{t}_{\mathrm{s}}(\llbracket \boldsymbol{u} \rrbracket) \tag{8}$$

represents an admissible choice (see [21, 22]). Following the notation as introduced in Section 2, $\boldsymbol{t}^{+}$ denotes the right hand limit of the traction vector.

Two different concepts suitable for the development of a constitutive law of the type (8) can be applied. According to SIMO, OLIVER & ARMERO [13], a projection of a classical stress-strain relationship onto the singular surface $\partial_{\mathrm{s}}\Omega$ leads to a material model characterized by Equation (8). Alternatively, a traction-separation law can be derived by assuming a singular distributed stored energy functional Ψ (see e.g. [15, 30]). In this paper, we follow the second concept.

Postulating an additive split of the stored energy, a functional of the format

$$\Psi = \Psi_{\mathrm{reg}} + \Psi_{\mathrm{in}}\ \delta_{\mathrm{s}} \tag{9}$$

is considered, cf. [14, 30, 34]. In Equation (9), Ψ_{reg} represents the regularly distributed part of the stored energy corresponding to points in $\Omega^{\pm}$, while Ψ_{in} denotes the singular part associated with points in $\partial_{\mathrm{s}}\Omega$. Assuming $\llbracket \boldsymbol{u} \rrbracket$ to be associated only with inelastic deformations, Ψ_{in} is specified by $\Psi_{\mathrm{in}} = \Psi_{\mathrm{in}}(\boldsymbol{\alpha}(\llbracket \boldsymbol{u} \rrbracket))$ in terms of the displacement-like internal variable $\boldsymbol{\alpha} \in \mathbb{R}^n$ depending on the displacement discontinuity. Similarly to standard plasticity [35], the space of admissible stresses

$$\mathbb{E}_{\boldsymbol{t}} := \left\{ (\boldsymbol{t}^{+}, \boldsymbol{q}) \in \mathbb{R}^3 \times \mathbb{R}^n \mid \phi(\boldsymbol{t}^{+}, \boldsymbol{q}) \leq 0 \right\} \quad \forall \boldsymbol{X} \in \partial_{\mathrm{s}}\Omega \tag{10}$$

is defined by means of a yield (failure) function $\phi(\boldsymbol{t}^{+}, \boldsymbol{q})$, which depends on the traction vector $\boldsymbol{t}^{+}$ and a vector of stress-like hardening/softening parameters $\boldsymbol{q}$ conjugated to $\boldsymbol{\alpha}$. For the special choice $\boldsymbol{\alpha} = \llbracket \boldsymbol{u} \rrbracket$ and $\phi(\boldsymbol{t}^{+}, \boldsymbol{q}) = ||\boldsymbol{t}^{+} - \boldsymbol{q}||$, $\boldsymbol{q} = \boldsymbol{t}_{\mathrm{s}}$ and $\phi = 0$ is equivalent to the condition of continuity of the traction vector. That is, the compatibility condition (7) can be rewritten as an equation which is formally identical to the necessary condition of yielding ($\phi = 0$) known from standard plasticity theory. Hence, Equation (7) is included in the more general space of admissible stresses. Since $\boldsymbol{t}_{\mathrm{s}}$ is included in the stress-like variable $\boldsymbol{q}$, the $+$ sign indicating the right hand side limit is omitted without risk of confusion, i.e. $\boldsymbol{t} := \boldsymbol{t}^{+}$.

Example 1: kinematic hardening/softening. For the special choices

$$\begin{aligned} \boldsymbol{q} = \boldsymbol{t}_{\mathrm{s}} \quad \text{and} \quad \phi : \mathbb{R}^3 \times \mathbb{R}^3 &\rightarrow \mathbb{R} \\ (\boldsymbol{t}, \boldsymbol{q}) &\mapsto ||\boldsymbol{t} - \boldsymbol{q}|| - t_{\mathrm{eq}}^{\mathrm{ini}} \end{aligned} \tag{11}$$

a kinematic hardening/softening of the yield surface ϕ is obtained. In Equation (11), $t_{\mathrm{eq}}^{\mathrm{ini}}$ represents a one-dimensional equivalent stress defining the initial admissible stress space and $||\bullet||$ denotes a norm (e.g. the standard Euclidean norm). Clearly, the shape of the yield function is defined by the choice of the norm.

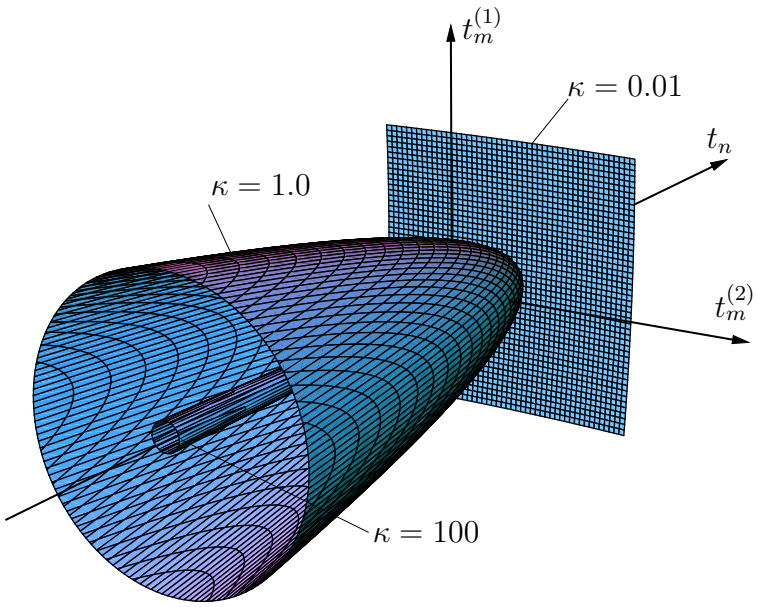

Figure 2: 3-D constitutive model for the analysis of mixed-mode material failure ($n = 2$): Adopted yield surface $\phi = 0$ in the t_n-$t_m^{(1)}$-$t_m^{(2)}$-space for different values of κ (see Equation (15)).

Example 2: isotropic hardening/softening. Setting

$$q = ||\boldsymbol{t}_{\mathrm{s}}|| \quad \text{and} \quad \begin{array}{rcl} \phi : \mathbb{R}^3 \times \mathbb{R}_+ & \rightarrow & \mathbb{R} \\ (\boldsymbol{t}, q) & \mapsto & ||\boldsymbol{t}|| - q, \end{array} \tag{12}$$

the isotropic case is received. Again, the shape of the yield function is defined by the norm.

Example 3: a mixed-mode material model. The numerical analyses presented in the following sections are based on a mixed-mode material model. To develop the yield function of this model, a local CARTESIAN coordinate system at $\boldsymbol{X}_0 \in \partial_{\mathrm{s}}\Omega$ is introduced. With

$$\boldsymbol{N}, \boldsymbol{M}^{(1)}, \boldsymbol{M}^{(2)} \in \mathcal{S}^2 := \{\boldsymbol{X} \in \mathbb{R}^3 \mid ||\boldsymbol{X}||_2 = 1\} \quad \text{and} \quad \left(\boldsymbol{M}^{(1)} \times \boldsymbol{M}^{(2)}\right) \cdot \boldsymbol{N} = 1, \tag{13}$$

the stress vector $\boldsymbol{t}$ is decomposed into its components

$$t_n := (\boldsymbol{N} \otimes \boldsymbol{N}) : \boldsymbol{\sigma}, \quad t_m^{(i)} := \left(\boldsymbol{N} \otimes \boldsymbol{M}^{(i)}\right) : \boldsymbol{\sigma}, \quad 1 \leq i \leq 2. \tag{14}$$

Using Equations (14), a yield function of the format

$$\phi(\boldsymbol{t}, \kappa, q) = t_n + \kappa \left[(t_m^{(1)})^2 + (t_m^{(2)})^2\right]^n - q \tag{15}$$

is adopted (see Figure (2)). For the two-dimensional case, a similar function ϕ has been proposed in [36]. According to Equation (15), the failure criterion is additively decomposed into a part associated with model-I fracture (t_n) and one part taking mode-II or mode-III failure into account ($t_m^{(\alpha)}$). The internal variables κ and q control the expansion of $\mathbb{E}_{\boldsymbol{t}}$ and the translation, respectively. The interaction between mode-I and mode-II failure is governed by κ and the constant parameter n.

Example 4: the limiting cases of the mixed-mode material model. As illustrated in Figure 2, in the limiting case $\kappa \to \infty$, the shear components of the traction vector have to vanish. Consequently, the admissible stress space degenerates to

$$\mathbb{E}_{\boldsymbol{t}} := \left\{ (\boldsymbol{t}, q) \in \mathbb{R}^3 \times \mathbb{R}_+ \;\middle|\; \phi_n := t_n - q \leq 0 \;\wedge\; t_m^{(i)} = 0 \quad 1 \leq i \leq 2 \right\}. \tag{16}$$

This stress space has been proposed in [16]. It is characterized by vanishing shear components of the traction vector $\boldsymbol{t}$. The other limiting case ($\kappa \to 0$) is equivalent to the RANKINE criterion. cf. Figure 2.

Since the space of admissible stresses (10) is formally identical to that of classical plasticity theory, the evolution equations defining the interface law can be derived similarly to those of their stress-strain based continuous counterpart. By introducing two potentials $g(\boldsymbol{t}, \boldsymbol{q})$ and $h(\boldsymbol{t}, \boldsymbol{q})$, the rates of $[\![\boldsymbol{u}]\!]$ and $\boldsymbol{\alpha}$ are postulated as

$$[\![\dot{\boldsymbol{u}}]\!] := \lambda \, \partial_{\boldsymbol{t}} g \quad \text{and} \quad \dot{\boldsymbol{\alpha}} = \lambda \, \partial_{\boldsymbol{q}} h \quad \text{with} \quad \partial_{\boldsymbol{t}} g := \frac{\partial g}{\partial \boldsymbol{t}}. \tag{17}$$

Analogously to standard plasticity, the plastic multiplier λ is computed from the consistency condition $\dot{\phi} = 0$. For the special choice $g = \phi$ and $h = \phi$, associative evolution equations are obtained. In this case, the rates (17) result from the principle of maximum dissipation. With the energy functional (9), the dissipation inequality (see [15, 21, 30, 37]) reads

$$\mathcal{D} = \boldsymbol{t} \cdot [\![\dot{\boldsymbol{u}}]\!] + \boldsymbol{q} \cdot \dot{\boldsymbol{\alpha}} \geq 0. \tag{18}$$

Hence, the postulate of maximum dissipation yields

$$\max_{\boldsymbol{t}, \boldsymbol{q}} \mathcal{D}|_{\mathbb{E}_{\boldsymbol{t}}}. \tag{19}$$

According to [38], the solution of the constraint maximization problem (19) is equivalent to the (local) KARUSH-KUHN-TUCKER-conditions of the LAGRANGE-functional

$$\mathcal{L}(\boldsymbol{t}, \boldsymbol{q}, \lambda) = -\mathcal{D} + \lambda \, \phi(\boldsymbol{t}, \boldsymbol{q}). \tag{20}$$

These conditions are computed as

$$[\![\dot{\boldsymbol{u}}]\!] = \lambda \, \partial_{\boldsymbol{t}} \phi, \quad \dot{\alpha} = \lambda \, \partial_{\boldsymbol{q}} \phi, \tag{21}$$

and

$$\lambda \geq 0, \quad \phi(\boldsymbol{t}, \boldsymbol{q}) \leq 0, \quad \lambda \, \phi(\boldsymbol{t}, \boldsymbol{q}) = 0. \tag{22}$$

In what follows, and according to standard notation in continuum mechanics, λ is referred to as the plastic multiplier.

The numerical analyses contained in the following sections are based on an associative model using the yield function (15). The evolution equations and their derivatives necessary for the numerical implementation are summarized in the appendix of this paper.

4 NUMERICAL IMPLEMENTATION

This section contains the numerical implementation of the constitutive model proposed in Section 3. The algorithmic formulation is restricted to the material point level (see [16, 21, 30, 39, 40]). In contrast to previous works [16, 21, 30, 40], the most general framework is presented. Referring to the yield function ϕ and the evolution equations, no special assumption is necessary.

4.1 Kinematics

According to Equation (3), the displacement field is decomposed into a smooth mapping $\bar{\boldsymbol{u}}$ and into a discontinuous part. The second part is further decomposed into the displacement jump $[\![\boldsymbol{u}]\!]$ and the discontinuous function $H_{\mathrm{s}} - \varphi$.

Analogously to standard continuum models, the continuous field $\bar{\boldsymbol{u}}$ is approximated globally conforming by using the shape functions N_i associated with node i of the respective finite element as

$$\bar{\boldsymbol{u}} \approx \sum_{i=1}^{n_{\mathrm{node}}} N_i \, \bar{\boldsymbol{u}}_i^e \quad \Rightarrow \quad \boldsymbol{\nabla}\bar{\boldsymbol{u}} \approx \sum_{i=1}^{n_{\mathrm{node}}} \bar{\boldsymbol{u}}_i^e \otimes \boldsymbol{\nabla} N_i. \tag{23}$$

In Equation (23), n_{node} denotes the number of nodes per finite element and $\bar{\boldsymbol{u}}_i^e$ represents the displacement vector at node i.

The discontinuous part of the displacement field characterized by the term $[\![\boldsymbol{u}]\!]\ (H_{\mathrm{s}} - \varphi)$ depends on the ramp function φ. As already mentioned in Section 2, φ has to comply with the restriction

$$\boldsymbol{u}(\boldsymbol{X}) = \bar{\boldsymbol{u}}(\boldsymbol{X}) \quad \forall \boldsymbol{X} \in \boldsymbol{X}_i^{\mathrm{e}}, \tag{24}$$

with $\boldsymbol{X}_i^{\mathrm{e}}$ denoting the position vectors of the element nodes. That is, the mapping φ allows to prescribe the DIRICHLET boundary conditions in terms of $\bar{\boldsymbol{u}}$. Most frequently, φ is specified by

$$\varphi = \sum_{i=1}^{n_{\Omega+}} N_i, \tag{25}$$

cf. [14, 16, 21, 22, 30]. In Equation (25), the summation has to be carried out over all nodes belonging to Ω^+. Figure 3 shows two possible modes of the function $H_{\mathrm{s}} - \varphi$ for a 4-node quadrilateral finite element. For higher order elements or for three-dimensional finite elements

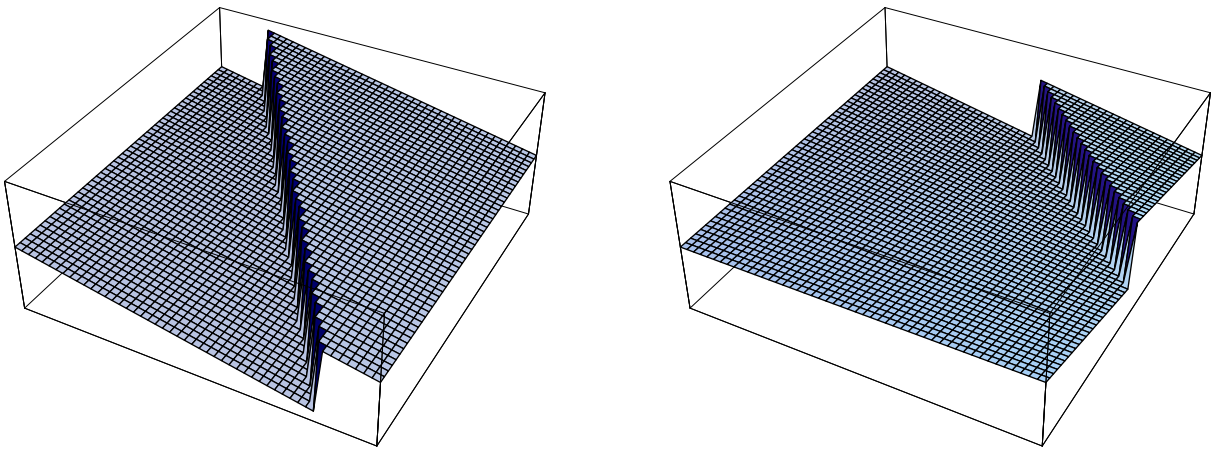

a) b)

Figure 3: Two possible modes of the discontinuous shape function $H_{\mathrm{s}} - \varphi$ using bi-linear functions. a) A localization surface is cutting two opposite edges of the finite element, b) a localization surface is cutting two adjacent edges of the finite element.

the development of the approximated discontinuous displacement field follows identical lines (see [16, 30, 41]). The displacement field is completed by the computation of the normal $\boldsymbol{N}$ ($\varphi = \varphi(\boldsymbol{N})$, $H_{\mathrm{s}} = H_{\mathrm{s}}(\boldsymbol{N})$) and the determination of the displacement jump $[\![\boldsymbol{u}]\!]$. Both variables follow from the considered constitutive model and will be specified in Subsection 4.3.

4.2 Finite element formulation

According to SIMO & OLIVER [22], the SDA is based on the stationarity conditions

$$\begin{aligned} \int_{\Omega^e} \boldsymbol{\nabla}^{\mathrm{sym}} \bar{\boldsymbol{\eta}} : \boldsymbol{\sigma}(\bar{\boldsymbol{u}}, [\![\boldsymbol{u}]\!])\, \mathrm{d}V &= \int_{\Omega^e} \bar{\boldsymbol{\eta}} \cdot \boldsymbol{f}\, \mathrm{d}V + \int_{\Gamma^e_{\boldsymbol{\sigma}}} \bar{\boldsymbol{\eta}} \cdot \boldsymbol{t}^*\, \mathrm{d}\Gamma \\ \int_{\Omega^e} \tilde{\boldsymbol{\gamma}} : \boldsymbol{\sigma}(\bar{\boldsymbol{u}}, [\![\boldsymbol{u}]\!])\, \mathrm{d}V &= 0. \end{aligned} \tag{26}$$

In Equations (26), $\bar{\boldsymbol{\eta}}$ denotes a continuous test function, $\boldsymbol{f}$ body forces, $\boldsymbol{t}^*$ prescribed traction vectors acting on the NEUMANN boundary $\Gamma_{\boldsymbol{\sigma}}$, Ω^e the domain of the respective finite element e and $\tilde{\boldsymbol{\gamma}}$ the variations of the enhanced strains. Clearly, Equation $(26)_1$ represents the weak form of equilibrium, while Equations $(26)_2$ is the L_2 orthogonality condition, cf. [32, 33].

Following a GALERKIN-type approximation of the continuous displacement field (see Equation (23)), the test function $\bar{\boldsymbol{\eta}}$ is assumed as

$$\bar{\boldsymbol{\eta}} \approx \sum_{i=1}^{n_{\mathrm{node}}} N_i\, \bar{\boldsymbol{\eta}}_i^e \quad \Rightarrow \quad \boldsymbol{\nabla}\bar{\boldsymbol{\eta}} \approx \sum_{i=1}^{n_{\mathrm{node}}} \bar{\boldsymbol{\eta}}_i^e \otimes \boldsymbol{\nabla} N_i. \tag{27}$$

According to SIMO & OLIVER [22], the variations $\tilde{\boldsymbol{\gamma}}$ are specified by

$$\tilde{\boldsymbol{\gamma}} = -\frac{1}{V^e}\, \boldsymbol{\beta} \otimes \boldsymbol{N} + \frac{1}{A_{\mathrm{s}}}\, \boldsymbol{\beta} \otimes \boldsymbol{N}\, \delta_{\mathrm{s}}. \tag{28}$$

In Equation (28), $\boldsymbol{\beta}$ represent an arbitrary variation of the displacement discontinuity, $A_{\mathrm{s}} := \int_{\partial_{\mathrm{s}}\Omega} \mathrm{d}\Gamma$ and $V^e := \int_{\Omega^e} \mathrm{d}V$. By inserting Equation (28) into Equation $(26)_2$ and accounting for $\boldsymbol{\nabla}\, [\![\boldsymbol{u}]\!] = \boldsymbol{0}$, the identity

$$\frac{1}{V^e} \int_{\Omega^e} \boldsymbol{\sigma} \cdot \boldsymbol{N}\, \mathrm{d}V = \boldsymbol{t}_{\mathrm{s}}([\![\boldsymbol{u}]\!]) \tag{29}$$

is obtained, cf. [22]. That is, the L_2 orthogonality condition is equivalent to the weak form of traction continuity. Since the kinematics, i.e. Equation (6), has been purely derived from kinematical considerations and $\tilde{\boldsymbol{\gamma}}$ purely from statical conditions, this approach is often referred to as the statically and kinematically optimal nonsymmetric formulation (SKON), cf. [19]. It should be noted that the space spanned by the enhanced strains and associated with the variations of the enhanced strains are not identical. As a consequence, a PETROV-GALERKIN discretization of the enhanced strains is applied. This results in a nonsymmetric stiffness matrix, as it will be shown in the following subsection.

Focusing on constant strain elements for now, the weak form (29) is equivalent to its strong form. According to Section 3, this strong form can be rewritten as $\phi(\boldsymbol{t}, \boldsymbol{q}) = 0$. Hence, instead of Equations (26), the equivalent problem

$$\begin{aligned} \int_{\Omega^e} \boldsymbol{\nabla}^{\mathrm{sym}} \bar{\boldsymbol{\eta}} : \boldsymbol{\sigma}(\bar{\boldsymbol{u}}, [\![\boldsymbol{u}]\!])\, \mathrm{d}V &= \int_{\Omega^e} \bar{\boldsymbol{\eta}} \cdot \boldsymbol{f}\, \mathrm{d}V + \int_{\Gamma^e_{\boldsymbol{\sigma}}} \bar{\boldsymbol{\eta}} \cdot \boldsymbol{t}^*\, \mathrm{d}\Gamma \\ \phi(\boldsymbol{t}, \boldsymbol{q}) &= 0 \end{aligned} \tag{30}$$

is considered. However, this set of equations is formally identical to that of classical plasticity theory (see Remark 2). As a result, the standard return-mapping algorithm can be applied. An efficient algorithm will be presented in the following subsection.

As explained in Section 2, the discontinuous part of the displacement field is restricted to the element level or the material point level. Consequently, $\bar{\boldsymbol{u}}$ represents the only global displacement field. Hence, linearization of Equations (30) (with respect to the nodal displacements) required for a global solution strategy based on NEWTON's method results in

$$\int_{\Omega^e} \boldsymbol{\nabla}^{\mathrm{sym}} \bar{\boldsymbol{\eta}} : \mathbb{C}^{\mathrm{ep}} : \boldsymbol{\nabla}^{\mathrm{sym}} \Delta \bar{\boldsymbol{u}} \, \mathrm{d}V = \int_{\Omega^e} \bar{\boldsymbol{\eta}} \cdot \Delta \boldsymbol{f} \, \mathrm{d}V + \int_{\Gamma^e_{\boldsymbol{\sigma}}} \bar{\boldsymbol{\eta}} \cdot \Delta \boldsymbol{t}^* \, \mathrm{d}\Gamma, \tag{31}$$

with

$$\mathbb{C}^{\mathrm{ep}} := \frac{\mathrm{d}\boldsymbol{\sigma}}{\mathrm{d}\boldsymbol{\nabla}^{\mathrm{sym}} \bar{\boldsymbol{u}}}. \tag{32}$$

The stress update as well as the computation of the algorithmic tangent moduli $\mathbb{C}^{\mathrm{ep}}$ will be presented in the following section.

Remark 2: The set of Equations (30) is formally identical to that of standard plasticity theory, if an inelastic load step is considered. However, in the case of elastic unloading ($[\![\dot{\boldsymbol{u}}]\!] = \boldsymbol{0}$), the mechanical problem is defined uniquely by means of Equation $(30)_1$. Equation $(30)_2$ is not required. Consequently, even in this case, the proposed SDA is formally identical to standard plasticity theory (in the context of standard plasticity models, the yield condition $\phi = 0$ needs only to be enforced for inelastic loading steps).

Remark 3: For elements which are not based on a constant strain interpolation, the same solution strategy, as presented in this and the following section, can be applied as well. For further details, refer to [42, 43].

4.3 Integration of the constitutive equations: A return-mapping algorithm

Assuming the inelastic deformations to be restricted to $\partial_{\mathrm{s}}\Omega$, together with the compatibility condition $\boldsymbol{\sigma}^+ \cdot \boldsymbol{N} = \boldsymbol{t}_{\mathrm{s}}$, the updated stresses $\boldsymbol{\sigma}$ and the stress-like internal variables $\boldsymbol{q}$ at the end of the time interval $[t_n, t_{n+1}]$ are obtained as

$$\begin{aligned} \boldsymbol{\sigma}(t_{n+1}) =: \boldsymbol{\sigma}_{n+1} &= \mathbb{C} : (\boldsymbol{\nabla}^{\mathrm{sym}} \bar{\boldsymbol{u}}_{n+1} - \tilde{\boldsymbol{\varepsilon}}_{n+1}) \\ \boldsymbol{q}_{n+1} &= \boldsymbol{q}(\boldsymbol{\alpha}_{n+1}). \end{aligned} \tag{33}$$

With the definition of a trial state

$$\begin{aligned} \boldsymbol{\sigma}^{\mathrm{tr}}_{n+1} &:= \mathbb{C} : (\boldsymbol{\nabla}^{\mathrm{sym}} \bar{\boldsymbol{u}}_{n+1} - \tilde{\boldsymbol{\varepsilon}}_n) \\ \boldsymbol{q}^{\mathrm{tr}}_{n+1} &:= \boldsymbol{q}(\boldsymbol{\alpha}_n) \end{aligned} \tag{34}$$

characterized by purely elastic deformations ($\lambda = 0$, $[\![\dot{\boldsymbol{u}}]\!] = \boldsymbol{0}$), the discrete counterpart of the loading condition is given as

$$\phi(\boldsymbol{\sigma}^{\mathrm{tr}}_{n+1}, \boldsymbol{q}^{\mathrm{tr}}_{n+1}) =: \phi^{\mathrm{tr}}_{n+1} > 0. \tag{35}$$

If inelastic loading is signaled by $\phi^{\mathrm{tr}}_{n+1} > 0$ the return-mapping algorithm is performed (see [35]). For that purpose, we apply a backward-EULER integration to the evolution of the displacement jump $[\![\boldsymbol{u}]\!]$ and to the evolution of the displacement-like internal variable $\boldsymbol{\alpha}$ (see Equation (17)) leading to

$$\Delta\, [\![\boldsymbol{u}]\!]_{n+1} = \Delta\lambda_{n+1} \;\; \partial_{\boldsymbol{t}} g|_{n+1} \quad \text{and} \quad \Delta\boldsymbol{\alpha}_{n+1} = \Delta\lambda_{n+1} \;\; \partial_{\boldsymbol{q}} h|_{n+1}\,, \tag{36}$$

with $\Delta(\bullet) := (\bullet)_{n+1} - (\bullet)_n$. Using Equation $(36)_1$, the increment of the regularly distributed enhanced strains is obtained as

$$\Delta\tilde{\boldsymbol{\varepsilon}}_{n+1} = \Delta\lambda_{n+1} \underbrace{\left(\partial_{\boldsymbol{t}} g|_{n+1} \otimes \boldsymbol{\nabla}\varphi\right)^{\mathrm{sym}}}_{:= \boldsymbol{G}_{n+1}}. \tag{37}$$

From Equation (37), $(34)_1$, together with Equation $(33)_1$, the stresses can be reformulated into

$$\boldsymbol{\sigma}_{n+1} = \boldsymbol{\sigma}^{\mathrm{tr}}_{n+1} - \mathbb{C} : \boldsymbol{G}_{n+1}\, \Delta\lambda_{n+1}. \tag{38}$$

Introducing a residual defined by

$$\boldsymbol{R} := \left\{ \begin{array}{c} \boldsymbol{R}^{\tilde{\boldsymbol{\varepsilon}}} \\ \boldsymbol{R}^{\boldsymbol{\alpha}} \end{array} \right\} := \left\{ \begin{array}{c} -\tilde{\boldsymbol{\varepsilon}}_{n+1} + \tilde{\boldsymbol{\varepsilon}}_n + \Delta\tilde{\boldsymbol{\varepsilon}}_{n+1} \\ -\boldsymbol{\alpha}_{n+1} + \boldsymbol{\alpha}_n + \Delta\boldsymbol{\alpha}_{n+1} \end{array} \right\}, \tag{39}$$

the set of differential equations describing the constitutive model is transformed into the algebraic problem

$$\boldsymbol{R} = \boldsymbol{0} \wedge \phi_{n+1} = 0. \tag{40}$$

Note that the resulting set of algebraic equations (40) is formally identical to that of standard (continuous deformations) plasticity. Consequently, any computer code for plasticity models can directly be used as the framework for the proposed algorithmic formulation. The linearizations of the proposed algorithm resulting in the tangent $\mathbb{C}^{\mathrm{ep}}$ are contained in Appendix A.

So far, we have developed a numerical implementation suitable for any traction-separation law. Such a general numerical framework has not been presented in the literature. Now, we want to specify our algorithmic formulation for the associative mixed-mode model described in Section 3. For the sake of simplicity, the internal variable κ is assumed to be constant. Consequently, a yield function of the form

$$\phi(\boldsymbol{t}, q) = \boldsymbol{N} \cdot \boldsymbol{t} + \kappa \left[\left[\boldsymbol{M}^{(1)} \cdot \boldsymbol{t} \right]^2 + \left[\boldsymbol{M}^{(2)} \cdot \boldsymbol{t} \right]^2 \right]^n - q \tag{41}$$

is adopted. In this case, the simplifications

$$\partial^2_{q\boldsymbol{\sigma}} \phi = \boldsymbol{0}, \quad \frac{\partial^2 \phi}{\partial q^2} = 0, \quad \partial^2_{\boldsymbol{t}q} \phi = \boldsymbol{0} \tag{42}$$

hold. As a consequence, matrix $\boldsymbol{A}^{-1}$ (see Appendix A) degenerates into a diagonal matrix and its inverse $\boldsymbol{A}$ can be computed directly in a closed form. Introducing the so-called algorithmic moduli by

$$\boldsymbol{\Xi}^{-1} := \mathbb{C}^{-1} + \Delta\lambda_{n+1} \left. \left(\partial^2_{\boldsymbol{t}\otimes\boldsymbol{\sigma}} \phi \otimes \boldsymbol{\nabla}\varphi \right)^{\mathrm{sym}} \right|_{n+1}, \tag{43}$$

the algorithmic tangent moduli are simplified to

$$\mathbb{C}^{\mathrm{ep}} = \boldsymbol{\Xi} - \frac{\boldsymbol{\Xi} : \boldsymbol{G} \otimes \partial_{\boldsymbol{\sigma}} \phi : \boldsymbol{\Xi}}{\partial_{\boldsymbol{\sigma}} \phi : \boldsymbol{\Xi} : \boldsymbol{G} - D}. \tag{44}$$

Although associative evolution equations are used, linearization leads to a non-symmetric 4th-order tensor $\mathbb{C}^{\mathrm{ep}}$. This results directly from the PETROV-GALERKIN discretization of the enhanced strains [16, 30], cf. Subsection 4.2. Consequently, the proposed finite element formulation is characterized by a non-symmetric stiffness matrix and falls into the class of so-called statically and kinematically optimal non-symmetric approaches (SKON) (see [19]).

So far, we have not applied the material character of the localization surface ($\dot{\boldsymbol{N}} = \boldsymbol{0}$). Hence, the developed numerical framework holds for time independent localization surfaces ($\dot{\boldsymbol{N}} = \boldsymbol{0}$) as well as for rotating localization surfaces ($\dot{\boldsymbol{N}} \neq \boldsymbol{0}$). Assuming a time independent failure zone characterized by

$$\phi := \phi(\boldsymbol{t}, \boldsymbol{N}, \boldsymbol{M}^{(1)}, \boldsymbol{M}^{(2)}, q), \quad \dot{\boldsymbol{N}} = \dot{\boldsymbol{M}}^{(1)} = \dot{\boldsymbol{M}}^{(2)} = \boldsymbol{0}, \tag{45}$$

the derivatives of the yield function ϕ (and the derivatives of the two potentials g, h for non-associative models) with respect to the stresses are computed using the chain rule as

$$\partial_{\boldsymbol{\sigma}} \phi = \left(\partial_{\boldsymbol{t}} \phi \cdot \frac{\partial \boldsymbol{t}}{\partial \boldsymbol{\sigma}} \right)^{\mathrm{sym}} = \left(\partial_{\boldsymbol{t}} \phi \otimes \boldsymbol{N} \right)^{\mathrm{sym}}. \tag{46}$$

A corresponding simplification also holds for the second derivative $\partial^2_{\boldsymbol{t} \otimes \boldsymbol{\sigma}} \phi$. For the mixed-mode material model employed in the numerical analyses, the required derivatives are contained in Appendix B and Appendix C.

Remark 4: The vector $\boldsymbol{N}$ defining the orientation of the localization surface has to be computed. For that purpose, different concepts can be applied such as non-classical bifurcation analyses (see [13, 14, 37]) and stress-based criteria [17, 27]. In the numerical studies presented in Sections 5-7, we analyze cracking in brittle structures. Hence, we assume the crack normal to be identical to the maximum principal stress direction at the time of crack initiation.

Remark 5: As shown in [30, 39] (see also Subsection 4.2), the proposed finite element formulation, which is restricted to the GAUSS point level, is identical to the original SDA as suggested in [14, 22] for constant strain elements.

5 LOCKING EFFECTS IN STRONG DISCONTINUITY APPROACHES

This subsection contains a numerical study of a notched concrete beam using the algorithmic formulation, proposed in Section 4. For the analysis of cracking in brittle structures, the associative mixed-mode material model, described in Section 3, is employed. Furthermore, a time independent crack surface ($\dot{\boldsymbol{N}} = \boldsymbol{0}$) is assumed. The orientation of the localization surface, i.e. the vector $\boldsymbol{N}$, is assumed to be identical to the direction of the maximum principal stress at the time when cracking occurs ($\phi_{n+1} > 0$).

The geometry, the loading and boundary conditions of the beam and the material parameters are depicted in Figure 4. The finite element discretizations used for the numerical analyses are illustrated in Figure 5. Note that only constant strain triangle elements are used. As already mentioned in Remark 5, for these elements, the proposed algorithmic formulation is equivalent to that of the original SDA as suggested in [14, 22]. According to Figure 5, the edges of the first mesh are aligned with respect to the topology of the expected crack path. Contrariwise, the edges of the second mesh are completely unstructured. Loading on top of the beam was applied by incrementally increasing nodal displacements along the width of the loading platen. The softening behavior after onset of cracking is assumed to follow the exponential law

$$q(\alpha) = f_{\mathrm{tu}} \, \exp\left[-\alpha \, \frac{f_{\mathrm{tu}}}{\mathcal{G}_{\mathrm{f}}} \right], \tag{47}$$

where $\mathcal{G}_{\mathrm{f}}$ denotes the specific fracture energy of concrete in tension and f_{tu} is the uniaxial tensile strength of concrete. Convergence is checked according to the maximum norm of the residuals with a tolerance of 10^{-6}.

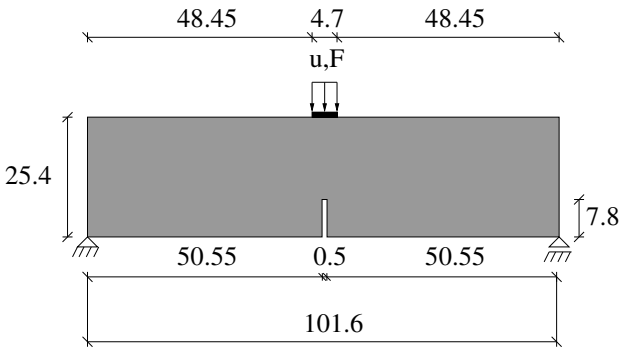

t	=	0.127	[m]
E	=	$4.36 \cdot 10^3$	[KN/cm^2]
ν	=	0.2	
f_{tu}	=	0.4	[KN/cm^2]
$\mathcal{G}_{\mathrm{f}}$	=	$1.195 \cdot 10^{-3}$	[KN cm/cm^2]

Figure 4: Numerical study of a notched concrete beam: Dimensions (in [cm]) and material parameters.

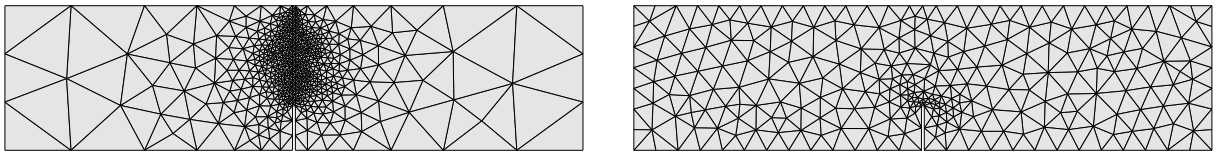

a) b)

Figure 5: Numerical study of a notched concrete beam: Finite element discretizations: a) 1222 constant strain triangle elements elements, b) 489 constant strain triangle elements.

Although the considered structure is relatively simple, it is well suited to demonstrate the locking effect resulting from different orientations of micro-defects and those of the corresponding macro-defects. Of course, more complex problems are more spectacular. However, such problems are characterized by different phenomena interacting with each other so that a physical meaningful analysis of the structural response is quite cumbersome. This is the reason for choosing the simple three-point bending test.

At first, the analysis is performed using the structured mesh. Figure 6 shows the distribution of the internal variable α representing the crack width ($\alpha = [\![\boldsymbol{u}]\!] \cdot \boldsymbol{N}$) for different values of κ. Independently of the parameter κ, a vertically oriented crack propagating along the symmetry

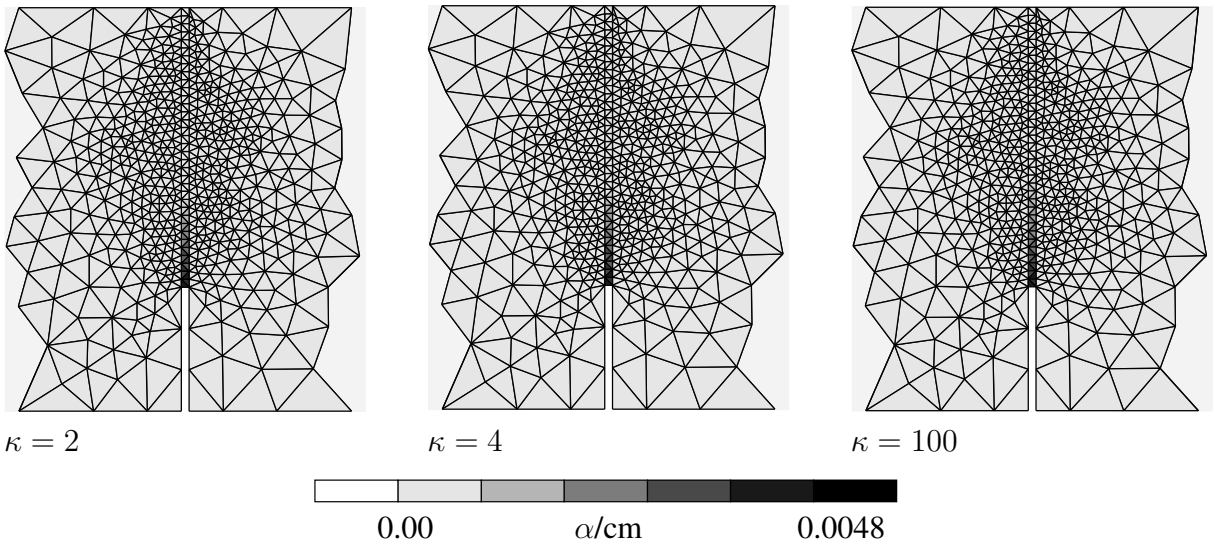

Figure 6: Numerical study of a notched concrete beam: Distribution of the internal variable $\alpha = [\![\boldsymbol{u}]\!] \cdot \boldsymbol{N}$ representing the crack width for different values of κ.

line starts to open. However, at a later stage of deformation, locking effects resulting occur. Furthermore, the smaller κ is, the earlier these problems arise. Consequently, it seems to be promising to study the limiting case $\kappa \to \infty$ (see Equation (16)). However, also in this case, it is impossible to compute the whole post peak structural response, since no convergence is obtained already at a relatively early stage after surpassing the ultimate load (see [16]).

Independently of κ, the direction of the maximum principal stress in the uncracked part of the beam in the vicinity of the crack tip is predicted to be orthogonal to the line of symmetry at an early stage of the analysis. As a consequence, the resulting crack surface is vertically oriented (see Remark 4). At a later stage of deformation, this direction rotates about 90°. Hence, a horizontally oriented micro-crack starts to open. It should be noted that this effect has been observed by several authors, cf. [16, 44, 45]. It occurs independently of the order of the displacement interpolation, cf. [16, 44]. Moreover, it is not restricted to SDA based finite element formulations. It has been observed using the X-FEM, cf. [44] and a discontinuous finite element model based on a numerical framework proposed by BOLZON & CORIGLIANO [46], cf. [45].

Assuming a fixed crack concept, the normal vector $\boldsymbol{N}$ is held constant during subsequent loading. Consequently, a wrong orientation of the resulting macro-crack is predicted. This leads to stress locking, as previously reported in [19]. In the presented analyses, the influence of these locking effects is very dominant so that no convergence is obtained at this time.

It is obvious that from a numerical point of view, the structured mesh, according to Figure 5a), represents the best case possible. In fact, the same locking effect, as already reported, has also been observed by using the unstructured mesh. However, for the sake of brevity, the respective results are not shown.

The numerical analyses presented in this section point out the necessity of a modification of the SDA. To overcome the described locking effect different advanced solution strategies have been proposed [19, 27]. In [19], the strong discontinuity approach has been coupled with a nonlocal damage model, while in [27] an extended finite element model (X-FEM) has been enhanced using a viscoplastic regularization. Both models capture the micro-defects by means of a continuous model (nonlocal damage theory or viscoplasticity). If a specific threshold is reached, a transition from the respective continuous model to the discontinuous model is applied. However, since the considered continuous models require a sufficiently fine resolution of the localization zone to guarantee mesh objectivity, the multiscale character of the underlying discontinuous approach is lost. Hence, both models result in high computational costs and consequently, they are less suitable for large-scale applications.

As an alternative, the discontinuous model itself can be modified. In the following sections, two different concepts will be proposed. Both approaches account for the multiscale character of the underlying physical problem and consequently, they are convenient for the numerical analysis of engineering structures.

6 ROTATING LOCALIZATION SURFACE APPROACH

In this section, rotating localization surfaces are assumed. Of course, if macro-defects such as fully opened cracks are considered, a rotating formulation would indeed be unphysical. However, the constitutive equations described in Section 3 and also the corresponding numerical implementation contained in Section 4 are applied to the modeling of macro-cracks as well as to the modeling of micro-cracks. These micro-cracks in fact do not rotate, but they are closing, while additional micro-cracks start opening. In this respect, the rotating formulation, which completely captures this phenomenon, seems reasonable (see [16, 30]). In contrast to previously

published works on this topic, the numerical framework which will be presented in this section is not restricted to a specific traction-separation law. The suggested finite element model can be applied to any plasticity based interface law as well as to a broad range of different damage type constitutive models.

As mentioned in Section 4, the proposed algorithmic formulation holds independently of the assumption of a time independent localization surface (except for Equations (45) and (46)). As a consequence, the numerical implementation of a rotating localization surface is included. Hence, the rotating localization surface approach is only presented in a brief form. For further details concerning this approach in the context of mode-I fracture, refer to [16, 21, 30].

Allowing the surface $\partial_{\mathrm{s}}\Omega$ to rotate, the yield function is postulated as

$$\phi := \phi(\boldsymbol{\sigma}, \boldsymbol{N}, \boldsymbol{M}^{(1)}, \boldsymbol{M}^{(2)}, q), \quad \text{with} \quad \dot{\boldsymbol{N}} \neq \boldsymbol{0},\ \dot{\boldsymbol{M}}^{(1)} \neq \boldsymbol{0},\ \dot{\boldsymbol{M}}^{(2)} \neq \boldsymbol{0}. \tag{48}$$

Thus, the CARTESIAN coordinate system $(\boldsymbol{N}, \boldsymbol{M}^{(1)}, \boldsymbol{M}^{(2)})$ depends on the state variables. For instance, a common assumption is represented by

$$\boldsymbol{N} = \boldsymbol{N}(\boldsymbol{\sigma}),\ \boldsymbol{M}^{(1)} = \boldsymbol{M}^{(1)}(\boldsymbol{\sigma}),\ \ \boldsymbol{M}^{(2)} = \boldsymbol{M}^{(2)}(\boldsymbol{\sigma}). \tag{49}$$

However, alternative hypotheses are suitable as well. Although the algorithmic formulation presented in Section 4 is applicable to the modeling of rotating localization surfaces, one modification has to be made. According to Equation (25), the discontinuous part of the displacement field depends on the shape functions associated with nodes belonging to Ω^+. Consequently, φ may vary during the return-mapping algorithm. However, since $\varphi(\boldsymbol{X}_0)$ represents a jump function with respect to time, the linearization $\partial\boldsymbol{\nabla}\varphi/\partial\boldsymbol{\sigma}$ required for the return-mapping algorithm cannot be computed (for further details, refer to [21]). For that purpose, we assume $\boldsymbol{\nabla}\varphi = \text{const}$. If the set of points belonging to Ω^+ does not change, this indeed represents the analytical solution. On the other hand, if $\partial_{\mathrm{s}}\Omega$ rotates by more than a geometrical threshold (φ changes) the assumption is wrong. In this case, the return-mapping algorithm is repeated with the updated function φ (see [16, 21]).

Now, the notched concrete beam is re-analyzed using the rotating localization approach. According to Section 5, the crack normal $\boldsymbol{N}$ is assumed to be identical to the maximum principal stress direction. As a consequence, we obtain

$$\boldsymbol{\sigma} : (\boldsymbol{N} \otimes \boldsymbol{N}) = \max_{1 \leq i \leq 3} \sigma_i \quad \text{with} \quad \boldsymbol{\sigma} = \sum_{i=1}^{3} \sigma_i\, \boldsymbol{N}_i \otimes \boldsymbol{N}_i. \tag{50}$$

Considering the coordinate system defined by the spectral decomposition (50), the shear stresses of the traction vector vanish, i.e.

$$\boldsymbol{\sigma} : (\boldsymbol{N} \otimes \boldsymbol{M}^{(i)}) = 0 \quad i \in \{1, 2\}. \tag{51}$$

Hence, for the proposed rotating localization surface approach, the yield function (41) simplifies to

$$\phi = (\boldsymbol{N} \otimes \boldsymbol{N}) : \boldsymbol{\sigma} - q. \tag{52}$$

Clearly, this result holds independently of the parameters n and κ, respectively. Except for the assumption of a rotating surface $\partial_{\mathrm{s}}\Omega$, the adopted constitutive law is identical to that employed in the numerical analyses in Section 5. The respective material parameters are summarized in Figure 4.

Figure 7 contains the load-displacement diagram resulting from the analyses of the notched concrete beam using the rotating crack formulation. According to Figure 7, and in contrast to

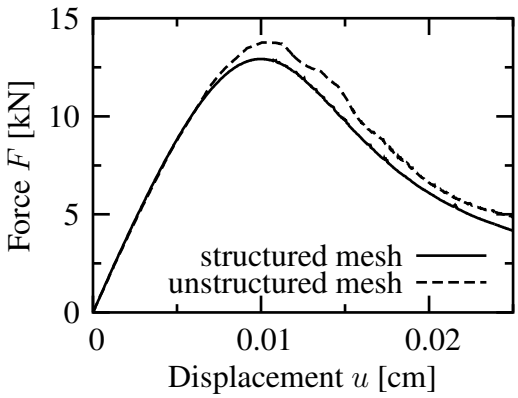

Figure 7: Numerical study of a notched concrete beam using the proposed rotating crack concept: Load-displacement diagrams obtained from the structured and the unstructured mesh.

the analyses based on the fixed crack concept, no convergence problems occur even in the post-peak regime. Although the unstructured mesh shows a relatively coarse discretization of the crack zone, both finite element meshes lead to similar results. This emphasizes the efficiency of the proposed algorithmic formulation.

The distribution of the internal variable $\alpha := \int_T [\![\boldsymbol{u}]\!] \cdot \boldsymbol{N} \, \mathrm{d}t$ computed from both meshes is illustrated in Figure 8. For both numerical analyses, a vertically oriented crack path is predicted.

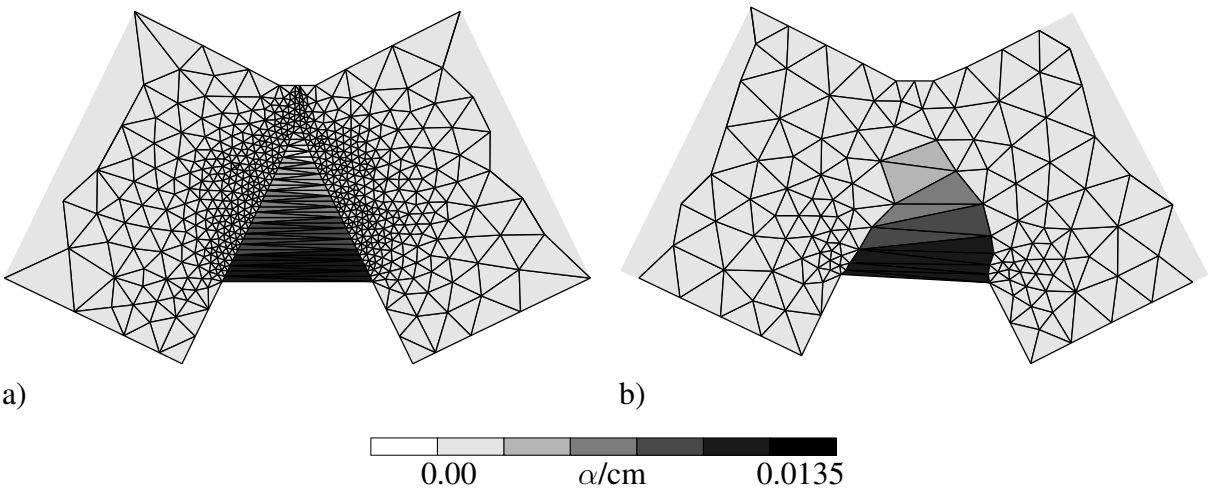

Figure 8: Numerical study of a notched concrete beam using the proposed rotating crack concept: Distribution of the internal variable α obtained from the structured a) and the unstructured mesh b) (at $u = 0.025$ cm, 1000-fold magnifications of the displacements).

It should be noted that the principal stresses computed in each GAUSS point do not exceed the uniaxial tensile strength of concrete ($f_{\mathrm{tu}} = 0.4$ kN/cm^2).

In this section, it was shown that allowing for rotations of the localization surface such as cracks, reduces the effect of stress locking. Furthermore, the rotating approach improves the robustness of failure analyses (see also [16, 21]). In contrast to previously published approaches, a relatively coarse discretization of the zone exhibiting localized deformations is sufficient to obtain physically meaningful results.

However, and in contrast to the fixed crack approach, the modeling of rotating discontinuities is only possible in an incompatible sense. As a consequence, crack path continuity cannot be enforced. Hence, this approach seems not to be promising for the extended finite element method.

7 MULTIPLE LOCALIZATION SURFACE APPROACH

This section deals with the modeling of intersecting localization surfaces which has, to the best knowledge of the author and with exception of [47], not been presented in the context of the strong discontinuity approach in the literature so far. However, the results published in [47] are based on single element studies. Furthermore, the respective numerical implementation has not been presented. In this section, we propose a multiple localization surface approach and its corresponding numerical implementation. Analogously to Section 4, the constitutive equations as well as the resulting finite element model can be applied to any plasticity based traction-separation law.

As shown in Section 5, the reported locking effect results from a misprediction of the normal vector $\boldsymbol{N}$ associated with the final macro-defect. More precisely, the vector $\boldsymbol{N}$ has been computed from the stress state corresponding to a micro-defect. However, as mentioned before, these micro-defects may close, while additional cracks start to open. Obviously, this cannot be modeled adequately by means of only one time invariant ($\dot{\boldsymbol{N}} = \boldsymbol{0}$) localization surface. In this section, an approach which completely avoids the described locking effect is presented. In contrast to the model proposed in the previous section, the assumption $\dot{\boldsymbol{N}} = \boldsymbol{0}$ is made, although the more general case can be implemented as well.

The main idea of the suggested multiple localization surface approach is to model each micro-defect separately by means of a singular surface. That is, the SDA is applied to predict the softening response associated with every micro-defect. If a specific threshold is reached, the micro-defect can be referred as to a macro-defect. However, a transition between the two different models (the one corresponding to the micro-defect and that used for the macro-defect) is not necessary.

In the following subsections, we start with the fundamentals of the multiple localization surface formulation. In this context, the most general case, n intersecting singular surfaces, is considered. No restrictions concerning the angle between these surfaces are imposed. Subsequently, the model is specified for the analysis of cracking in brittle materials.

7.1 Kinematics

Similarly to the single fixed crack approach, a displacement field of the type (3) is adopted. However, considering n localization surfaces within the respective finite element, Equation (3) results in

$$\boldsymbol{u} = \bar{\boldsymbol{u}} + \sum_{i=1}^{n} (H_{\mathrm{s}}^{(i)} - \varphi^{(i)}) \; [\![\boldsymbol{u}]\!]^{(i)} \,. \tag{53}$$

As a consequence, the strain field

$$\boldsymbol{\varepsilon} = \boldsymbol{\nabla}^{\mathrm{sym}} \bar{\boldsymbol{u}} - \sum_{i=1}^{n} \left([\![\boldsymbol{u}]\!]^{(i)} \otimes \boldsymbol{\nabla} \varphi^{(i)} \right)^{\mathrm{sym}} + \sum_{i=1}^{n} \left([\![\boldsymbol{u}]\!]^{(i)} \otimes \boldsymbol{N}^{(i)} \right)^{\mathrm{sym}} \; \delta_{\mathrm{s}}^{(i)} \tag{54}$$

is assumed, where $\boldsymbol{N}^{(i)}$ represents the normal of the crack surface i, $[\![\boldsymbol{u}]\!]^{(i)}$ the corresponding displacement discontinuity and $\delta_{\mathrm{s}}^{(i)}$ the DIRAC delta distribution associated with localization surface i, respectively.

7.2 Constitutive equations

Analogously to Section 3, the material response is governed by means of traction-separation laws. Following identical lines as proposed in Section 3, these interface laws capturing the

softening response associated with the localization surface i are based on admissible stress states defined as

$$\mathbb{E}_{\boldsymbol{t}}^{(i)} := \{(\boldsymbol{t}^{(i)}, \boldsymbol{q}^{(i)}) \in \mathbb{R}^3 \times \mathbb{R}^n \mid \phi^{(i)}(\boldsymbol{t}^{(i)}, \boldsymbol{q}^{(i)}) \leq 0\}, \quad \text{with} \quad \boldsymbol{t}^{(i)} := \boldsymbol{\sigma} \cdot \boldsymbol{N}^{(i)} \tag{55}$$

and on the evolution equations

$$\begin{array}{rcl} [\![\dot{\boldsymbol{u}}]\!]^{(i)} & = & \lambda^{(i)}\, \partial_{\boldsymbol{t}^{(i)}} g^{(i)} \\ \dot{\boldsymbol{\alpha}}^{(i)} & = & \lambda^{(i)}\, \partial_{\boldsymbol{q}^{(i)}} h^{(i)}, \end{array} \tag{56}$$

respectively (compare with Section 3). According to Section 3, $g^{(i)} = g^{(i)}(\boldsymbol{t}^{(i)}, \boldsymbol{q}^{(i)})$ and $h^{(i)} = h^{(i)}(\boldsymbol{t}^{(i)}, \boldsymbol{q}^{(i)})$ represent two potentials and $\lambda^{(i)}$ denotes a plastic multiplier. Consequently, the constitutive laws suggested in Section 3 can be applied without any modification to each localization surface i. Since the restriction $(\boldsymbol{t}^{(i)}, \boldsymbol{q}^{(i)}) \in \mathbb{E}_{\boldsymbol{t}}^{(i)}$ has to be fulfilled for all $i \in \{1, \ldots, n\}$, the admissible stress space $\mathbb{E}_{\boldsymbol{t}}$ is defined as the intersection of all subspaces $\mathbb{E}_{\boldsymbol{t}}^{(i)}$, i.e.

$$\mathbb{E}_{\boldsymbol{t}} := \bigcap_{i=1}^{n} \mathbb{E}_{\boldsymbol{t}}^{(i)}. \tag{57}$$

7.3 Numerical implementation

Following Subsection 4.3, the proposed numerical implementation is based on an implicit backward-EULER integration, together with a local NEWTON iteration, and results in a so-called return-mapping algorithm.

With the introduction of a trial-state in standard fashion (see Section 4.3), the stresses at time t_{n+1} are obtained as

$$\boldsymbol{\sigma}_{n+1} = \boldsymbol{\sigma}_{n+1}^{\mathrm{tr}} - \mathbb{C} : \left\{ \sum_{i \in \mathbb{J}_{\mathrm{act}}} \left(\partial_{\boldsymbol{t}^{(i)}} g^{(i)} \otimes \boldsymbol{N}^{(i)} \right)^{\mathrm{sym}} \Delta\lambda^{(i)} \right\} \Bigg|_{n+1}. \tag{58}$$

According to multisurface plasticity, $\mathbb{J}_{\mathrm{act}}$ denotes the set of all active constraints. Consequently, the starting set of $\mathbb{J}_{\mathrm{act}}$ is defined as

$$\mathbb{J}_{\mathrm{act}}^{\mathrm{tr}} := \left\{ i \in \{1, \ldots, n\} \mid \phi^{(i)\mathrm{tr}} > 0 \right\}. \tag{59}$$

However, the condition $\phi^{(i)\mathrm{tr}} > 0$ does not guarantee that the surface $\phi^{(i)}$ is ultimately active. Hence, the set of active constraints has to be updated within the return-mapping algorithm. For further details, refer to [35].

Applying a backward-EULER integration to the evolution Equations (56), the nonlinear set of differential equations describing the constitutive law is transformed into the algebraic problem

$$\phi_{n+1}^{(i)} = 0 \ \wedge \ \boldsymbol{R} = \boldsymbol{0} \quad \forall i \in \mathbb{J}_{\mathrm{act}}, \tag{60}$$

with the residuals

$$\boldsymbol{R} := \left\{ \begin{array}{c} \boldsymbol{R}^{\tilde{\boldsymbol{\varepsilon}}} \\ \boldsymbol{R}^{\boldsymbol{\alpha}} \end{array} \right\} := \left\{ \begin{array}{c} -\tilde{\boldsymbol{\varepsilon}}_{n+1} + \tilde{\boldsymbol{\varepsilon}}_n \\ -\boldsymbol{\alpha}_{n+1} + \boldsymbol{\alpha}_n \end{array} \right\} + \sum_{i \in \mathbb{J}_{\mathrm{act}}} \Delta\lambda^{(i)} \left\{ \begin{array}{c} \partial_{\boldsymbol{t}^{(i)}} g^{(i)} \\ \partial_{\boldsymbol{q}^{(i)}} h^{(i)} \end{array} \right\} \Bigg|_{n+1}. \tag{61}$$

The solution of the nonlinear set of Equations (60) is computed using NEWTON's method. For that purpose the linearization of Equations (60) is required. However, they follow identical

lines as shown in Section 4.3. The resulting numerical implementation is formally identical to the standard multisurface plasticity return-mapping algorithm for non-associative models (see [35]).

Remark 6: The presented implementation is based on the determination of the set $\mathbb{J}_{\mathrm{act}}$. This set of active constraints is computed according to [35]. As reported by several authors, this procedure may lead to numerical problems. However, such problems have not been observed in the presented analyses. Clearly, in the case of a large number of potential active singular surfaces other algorithms are more convenient. In fact, almost every numerical procedure known from computational single crystal plasticity can be applied to the presented SDA as well. Particularly, algorithms based on an augmented Lagrangian formulation seems to be promising, cf. [48].

Remark 7: According to Remark 4, the vector $\boldsymbol{N}$ defining the orientation of the localization surface has to be computed. Most frequently, $\boldsymbol{N}$ is determined by means of non-classical bifurcation analyses (see [13, 14, 37]) or stress-based criteria [17, 27]. If one specific criterion is chosen, the orientation of the first activated localization surface can be computed in standard manner leading to $\boldsymbol{N}^{(1)}$. It is canonical to apply the same criterion to compute the normal vector $\boldsymbol{N}$ of any further localization surface. That is, within each time step, the orientation of a new potential localization surface (number i) is computed first. Subsequently, it is checked, if this surface is active, i.e. $\phi^{(i)} > 0$. If this is the case and the angle between $\boldsymbol{N}^{(i)}$ and the already existing normal vectors is greater than a prescribed tolerance, a new localization surface is introduced.

7.4 A multiple localization surface model based on a mixed-mode material model

In what follows, we summarize the specific constitutive law which will be used in the numerical analyses based on the multiple localization surface approach. Assuming plane stress conditions, two intersecting cracks defined by their corresponding unit normal vectors $\boldsymbol{N}^{(1)}$ and $\boldsymbol{N}^{(2)}$ are allowed to propagate within the respective finite element. The corresponding tangential vectors are denoted as $\boldsymbol{M}^{(1)}$ and $\boldsymbol{M}^{(2)}$. The admissible angle between the localization surfaces is restricted by the criterion $\angle(\boldsymbol{N}^{(1)}, \boldsymbol{N}^{(2)}) > 45^{\circ}$.

Analogously to Section 5, a yield function of the type (41) is adopted. This failure function is employed for both localization surfaces. That is, we make the natural assumption that each crack is governed by the same physical mechanism. As a consequence, the admissible stress space is defined by

$$\mathbb{E}_{\boldsymbol{t}} := \{(\boldsymbol{\sigma}, q^{(1)}, q^{(2)}) \in \mathbb{R}^3 \times \mathbb{R}_+ \times \mathbb{R}_+ \mid \phi^{(1)} \leq 0,\ \phi^{(2)} \leq 0\}, \tag{62}$$

with

$$\phi^{(i)}(\boldsymbol{t}^{(i)}, q^{(i)}(\alpha^{(i)})) = \boldsymbol{N}^{(i)} \cdot \boldsymbol{t}^{(i)} + \kappa \left[\boldsymbol{M}^{(i)} \cdot \boldsymbol{t}^{(i)}\right]^2 - q^{(i)}(\alpha^{(i)}), \quad i \in \{1;2\}. \tag{63}$$

In Equations (63), the notations

$$\boldsymbol{t}^{(i)} := \boldsymbol{\sigma} \cdot \boldsymbol{N}^{(i)} \qquad \alpha^{(i)} := [\![\boldsymbol{u}]\!]^{(i)} \cdot \boldsymbol{N}^{(i)} \qquad i \in \{1;2\} \tag{64}$$

have been used.

7.5 Numerical re-analysis of a notched concrete beam

This subsection contains a numerical re-analysis of the notched concrete beam (see Figure 4) using the multiple crack approach as proposed in this section. The material parameters are

chosen according to Figure 4. The parameter κ is set to 4. Hence, a mixed-mode material model is adopted.

Figure 9 contains the load-displacement diagrams resulting from the numerical analysis using the multiple localization surface approach. Similarly to the rotating SDA, no convergence

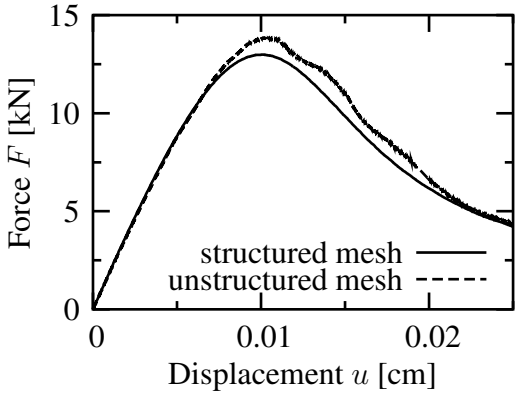

Figure 9: Numerical study of a notched concrete beam using the proposed multiple crack concept: Load-displacement diagram obtained from the structured and the unstructured mesh.

problems arise if intersecting cracks are allowed. According to Figure 9, although the unstructured mesh shows a relatively coarse discretization of the crack zone, both finite element meshes lead to similar results. This represents an important advantage of the proposed finite element model compared to other existing approaches.

For the purpose of comparison of the results obtained from the multiple localization formulation with those computed from rotating localization formulation, the respective load-displacement diagrams are shown in Figure 10 once again. In Figure 10a), the structural response

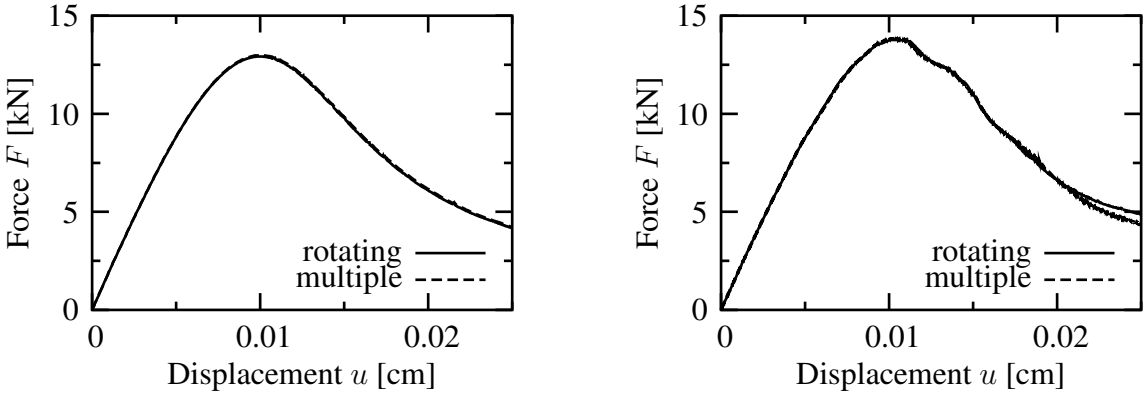

Figure 10: Numerical study of a notched concrete beam using the proposed multiple crack concept: Load-displacement diagram obtained from the structured and the unstructured mesh.

predicted by the structured mesh is illustrated. According to this figure, both approaches lead to almost identical results. The same holds for the unstructured discretization (Figure 10b)). Only at a later stage of deformation ($u > 0.2$ cm) a slight difference is observed.

Figure 11 contains the distribution of the internal variable $\alpha := \max(\alpha_1, \alpha_2)$ computed from the multiple SDA. By comparison of Figure 11 with Figure 8, it is concluded that both models lead to almost identical results. According to Figure 11, no stress locking is observed even for the unstructured discretization. The principal stresses computed in each integration point do not

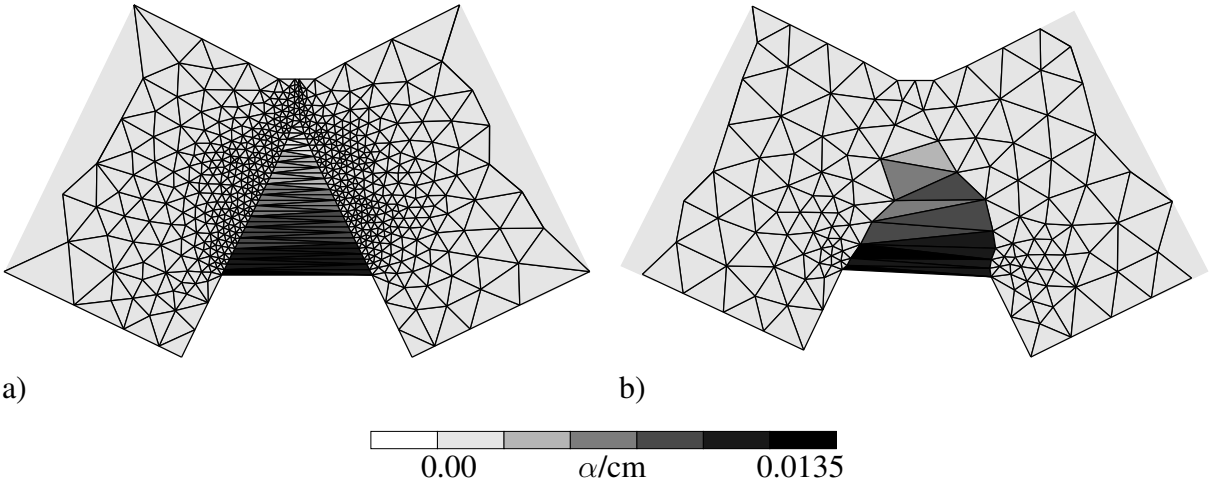

Figure 11: Numerical study of a notched concrete beam using the proposed multiple crack concept: Distribution of the internal variable $\alpha = \max(\alpha_1, \alpha_2)$ obtained from the structured a) and the unstructured mesh (at $u = 0.025$ cm, 1000-fold magnifications of the displacements)

exceed the uniaxial tensile strength of concrete ($f_{\mathrm{tu}} = 0.4$ kN/cm^2). It should be noted that in each element in which two localization surfaces are active, the angle between these surfaces is approximately about 90°, i.e. $\angle(\boldsymbol{N}^{(1)}, \boldsymbol{N}^{(2)}) \approx 90^\circ$.

In contrast to the rotating crack concept, the normal vectors $\boldsymbol{N}$ and $\boldsymbol{M}$ defining the intersecting localization surfaces of the multiple SDA are assumed as constant. Consequently, crack path continuity can be enforced. Hence, this approach is also suitable for other finite element models based on displacement discontinuities such as the extended finite element method. However, compared to the algorithmic formulation of the rotating SDA, the implementation of intersecting cracks is more complicated. On the one hand side, the numerical costs associated with multisurface plasticity models increase considerably compared to the implementation of single surface plasticity. In this context, the determination of the active constraints for softening materials has to be mentioned. On the other hand, allowing intersecting localization surfaces requires an efficient band tracing algorithm, if more realistic engineering problems are analyzed.

Remark 8: As mentioned in the introduction of the present section, the numerical analysis presented in this subsection is based on the assumption $\dot{\boldsymbol{N}} = \dot{\boldsymbol{M}} = \boldsymbol{0}$. However, and similarly to Subsection 4.3, the proposed numerical implementation of the multiple SDA also holds for rotating localization surfaces.

8 CONCLUSION

A finite element formulation based on the so-called strong discontinuity approach (SDA) suitable for large-scale failure analyses of elastoplastic solids has been presented in this paper. The proposed framework holds for arbitrary types of finite elements, including 3D elements, as well as for any plasticity based traction-separation law. For the analysis of cracking in concrete, a mixed-mode material model has been adopted. The corresponding constitutive equations have been incorporated into a constant strain triangle element.

From a numerical analysis of a notched concrete beam, it was shown that the proposed finite element formulation based on time independent localization surfaces leads to locking effects which result in convergence problems. These locking effects are caused by different orientations of micro-defects and those of the corresponding macro-defects. This deficiency of the presented

SDA also holds for other existing finite element models based on strong discontinuities such as the X-FEM.

To overcome these locking effects, two alternative models have been compared with each other: The rotating localization surface approach and the multiple localization surface approach. From a numerical re-analysis of the notched concrete beam, it was demonstrated that both advanced models agree with the experimentally observed crack pattern and eliminate the locking effect.

The rotating crack concept is characterized by a numerically robust implementation. However, allowing the crack to rotate, crack path continuity cannot be enforced and consequently, the discontinuous displacement field has to be modeled in an incompatible fashion. Hence, the rotating crack concept seems not to be promising for the extended finite element method. In contrast to the rotating SDA, the multiple SDA allows to enforce crack path continuity. As a consequence, this approach is also suitable for other discontinuous displacement field based finite element formulations. However, the resulting numerical costs increase drastically compared to the rotating crack concept, especially if band tracing algorithms are applied.

Acknowledgement

This work was completed under the financial support of the Deutsche Forschungsgemeinschaft (DFG) through project A4 under supervision of Prof. O.T. Bruhns within the Collaborative Research Centre 398. The author wishes to express his sincere gratitude to this support. Furthermore, the author would like to thank Prof. O.T. Bruhns for his helpful comments.

APPENDIX A

This appendix is concerned with the linearization of the return-mapping algorithm as proposed in Subsection 4.3.

According to standard procedures in computational mechanics, the solution of Equations (40) is computed using NEWTON's method. For that purpose, the linearizations of $\boldsymbol{R}$ and ϕ are required. With the second order tensor of the plastic moduli $\boldsymbol{D} := -\mathrm{d}\boldsymbol{q}/\mathrm{d}\boldsymbol{\alpha}$, the linearization of $\boldsymbol{R}^{\boldsymbol{\alpha}}$ results in

$$\begin{aligned}\mathrm{d}\boldsymbol{R}^{\boldsymbol{\alpha}} = \boldsymbol{D}_{n+1}^{-1} : \mathrm{d}\boldsymbol{q}_{n+1} + \mathrm{d}\Delta\lambda_{n+1}\ \partial_{\boldsymbol{q}} h\big|_{n+1} + \Delta\lambda_{n+1}\ \partial^2_{\boldsymbol{q}\otimes\boldsymbol{q}} h\big|_{n+1} \cdot \mathrm{d}\boldsymbol{q}_{n+1} \\ + \Delta\lambda_{n+1}\ \partial^2_{\boldsymbol{q}\otimes\boldsymbol{\sigma}} h\big|_{n+1} : \mathrm{d}\boldsymbol{\sigma}_{n+1}.\end{aligned} \tag{65}$$

Similarly, we obtain

$$\begin{aligned}\mathrm{d}\boldsymbol{R}^{\tilde{\boldsymbol{\varepsilon}}} = \mathbb{C}^{-1} : \mathrm{d}\boldsymbol{\sigma}_{n+1} + \mathrm{d}\Delta\lambda_{n+1}\ \left(\partial_{\boldsymbol{t}} g\big|_{n+1} \otimes \boldsymbol{\nabla}\varphi\right)^{\mathrm{sym}} \\ + \Delta\lambda_{n+1}\ \left(\partial^2_{\boldsymbol{t}\otimes\boldsymbol{\sigma}} g\big|_{n+1} \otimes \boldsymbol{\nabla}\varphi\right)^{\mathrm{sym}} : \mathrm{d}\boldsymbol{\sigma}_{n+1} \\ + \Delta\lambda_{n+1}\ \left(\partial^2_{\boldsymbol{t}\otimes\boldsymbol{q}} g\big|_{n+1} \otimes \boldsymbol{\nabla}\varphi\right)^{\mathrm{sym}} \cdot \mathrm{d}\boldsymbol{q}_{n+1}.\end{aligned} \tag{66}$$

In Equation (66), the identity $\mathrm{d}\boldsymbol{\sigma}_{n+1} = -\mathbb{C} : \mathrm{d}\tilde{\boldsymbol{\varepsilon}}_{n+1}$, which holds within a particular step of the return-mapping algorithm, has been applied. Note that the simple (double) contraction in Equation (66) is not the standard one, i.e.

$$\begin{aligned}\left[\left(\partial^2_{\boldsymbol{t}\otimes\boldsymbol{\sigma}} g \otimes \boldsymbol{\nabla}\varphi\right)^{\mathrm{sym}} : \mathrm{d}\boldsymbol{\sigma}\right]_{ij} &= \left(\partial^2_{t_i\sigma_{kl}} g\ \nabla\varphi_j\right)^{\mathrm{sym}}\ \mathrm{d}\sigma_{kl} \\ \left[\left(\partial^2_{\boldsymbol{t}\otimes\boldsymbol{q}} g \otimes \boldsymbol{\nabla}\varphi\right)^{\mathrm{sym}} \cdot \mathrm{d}\boldsymbol{q}\right]_{ij} &= \left(\partial^2_{t_i q_k} g \nabla\varphi_j\right)^{\mathrm{sym}}\ \mathrm{d}q_k.\end{aligned} \tag{67}$$

Combining Equation (65) with Equation (66), the linearization of $\boldsymbol{R}$ is written as

$$\mathrm{d}\boldsymbol{R} = \boldsymbol{A}^{-1}\ \boldsymbol{\Delta} + \mathrm{d}\Delta\lambda_{n+1}\ \boldsymbol{\nabla} M, \tag{68}$$

with

$$\boldsymbol{A}^{-1} := \begin{bmatrix} \mathbb{C}^{-1} + \Delta\lambda\ (\partial^2_{\boldsymbol{t}\otimes\boldsymbol{\sigma}} g \otimes \boldsymbol{\nabla}\varphi)^{\mathrm{sym}} & \Delta\lambda\ \partial^2_{\boldsymbol{t}\otimes\boldsymbol{q}} g \\ \Delta\lambda\ \partial^2_{\boldsymbol{q}\otimes\boldsymbol{\sigma}} h & \boldsymbol{D}^{-1} + \Delta\lambda \partial^2_{\boldsymbol{q}\otimes\boldsymbol{q}} h \end{bmatrix}, \quad \boldsymbol{\Delta} := \begin{bmatrix} \mathrm{d}\boldsymbol{\sigma}_{n+1} \\ \mathrm{d}\boldsymbol{q}_{n+1} \end{bmatrix} \tag{69}$$

and

$$\boldsymbol{\nabla} M^T := \left[\boldsymbol{G}_{n+1};\ \partial_{\boldsymbol{q}} h|_{n+1}\right]. \tag{70}$$

Defining

$$\boldsymbol{\nabla}\phi^T := \left[\partial_{\boldsymbol{\sigma}}\phi;\ \partial_{\boldsymbol{q}}\phi\right], \tag{71}$$

the increment of the plastic multiplier during an iteration cycle is obtained in matrix notation as (compare with [16, 30])

$$\mathrm{d}\Delta\lambda_{n+1} = \frac{\phi_{n+1} - \boldsymbol{\nabla}\phi^T\ \boldsymbol{A}\ \boldsymbol{R}}{\boldsymbol{\nabla}\phi^T\ \boldsymbol{A}\ \boldsymbol{\nabla} M}. \tag{72}$$

Following the standard return-mapping algorithm as proposed in [35], the algorithmic tangent tensor required for a globally convergent behavior at an asymptotic rate is computed as (see [16, 21])

$$\mathbb{C}^{\mathrm{ep}} = \left.\frac{\mathrm{d}\boldsymbol{\sigma}}{\mathrm{d}\boldsymbol{\nabla}^{\mathrm{sym}}\bar{\boldsymbol{u}}}\right|_{n+1} = \boldsymbol{A}_{[11]} - \frac{\{\boldsymbol{A}\ \boldsymbol{\nabla} M \otimes \boldsymbol{\nabla}\phi^T\ \boldsymbol{A}\}_{[11]}}{\boldsymbol{\nabla}\phi^T\ \boldsymbol{A}\ \boldsymbol{\nabla} M}. \tag{73}$$

In Equation (73), the abbreviation $[\bullet]_{11}$ indicating the submatrix 11 has been used.

APPENDIX B

This appendix contains a brief summary of a three-dimensional mixed-mode material model based on discontinuous displacement fields. The two-dimensional counterpart is summarized in Appendix C. In addition to the equations defining the constitutive model such as the yield function and the evolution equations, their derivatives required for the numerical implementation are given as well.

According to Section 3, a local CARTESIAN coordinate system at $\boldsymbol{X}_0 \in \partial_{\mathrm{s}}\Omega$ is introduced

$$\boldsymbol{N}, \boldsymbol{M}^{(1)}, \boldsymbol{M}^{(2)} \in \mathcal{S}^2 := \{\boldsymbol{X} \in \mathbb{R}^3 \mid ||\boldsymbol{X}||_2 = 1\} \quad \text{and} \quad \left(\boldsymbol{M}^{(1)} \times \boldsymbol{M}^{(2)}\right) \cdot \boldsymbol{N} = 1. \tag{74}$$

With the decomposition of the stress vector $\boldsymbol{t}$ into its components

$$t_n := (\boldsymbol{N} \otimes \boldsymbol{N}) : \boldsymbol{\sigma}, \quad t_m^{(i)} := \left(\boldsymbol{N} \otimes \boldsymbol{M}^{(i)}\right) : \boldsymbol{\sigma} \quad 1 \le i \le 2, \tag{75}$$

a yield function of the form

$$\phi(\boldsymbol{t}, \kappa, q) = t_n + \kappa\ \left[(t_m^{(1)})^2 + (t_m^{(2)})^2\right]^n - q \tag{76}$$

is adopted. Substitution of Equations (75) in Equation (76) yields

$$\phi(\boldsymbol{t}, \kappa, q) = (\boldsymbol{N} \otimes \boldsymbol{N}) : \boldsymbol{\sigma} + \kappa\ \left[\left[\left(\boldsymbol{N} \otimes \boldsymbol{M}^{(1)}\right) : \boldsymbol{\sigma}\right]^2 + \left[\left(\boldsymbol{N} \otimes \boldsymbol{M}^{(2)}\right) : \boldsymbol{\sigma}\right]^2\right]^n - q. \tag{77}$$

Here, $\kappa = \kappa(\alpha_1)$ and $q = q(\alpha_2)$ represent internal variables conjugated to $\alpha_1 = \alpha_1(\llbracket \boldsymbol{u} \rrbracket)$ and $\alpha_2 = \alpha_2(\llbracket \boldsymbol{u} \rrbracket)$, respectively. Assuming an associative model, the evolution equations are obtained as

$$\dot{\alpha}_1 = \lambda \, \partial_\kappa \phi = \lambda \, \left[\left[\left(\boldsymbol{N} \otimes \boldsymbol{M}^{(1)} \right) : \boldsymbol{\sigma} \right]^2 + \left[\left(\boldsymbol{N} \otimes \boldsymbol{M}^{(2)} \right) : \boldsymbol{\sigma} \right]^2 \right]^n , \tag{78}$$

$$\dot{\alpha}_2 = \lambda \, \partial_q \phi = \lambda \tag{79}$$

and

$$\llbracket \dot{\boldsymbol{u}} \rrbracket = \lambda \, \partial_{\boldsymbol{t}} \phi = \lambda \, \left[\boldsymbol{N} + 2 \, n \, \kappa \, \left[(t_m^{(1)})^2 + (t_m^{(2)})^2 \right]^{n-1} \, \left(t_m^{(1)} \, \boldsymbol{M}^{(1)} + t_m^{(2)} \, \boldsymbol{M}^{(2)} \right) \right] , \tag{80}$$

with the plastic multiplier λ. Applying the return-mapping algorithm to solve the set of differential equations describing the considered constitutive model, the linearization of Equation (80) is required. Using

$$\begin{aligned} \partial^2_{\boldsymbol{t} \otimes \boldsymbol{\sigma}} \phi = & \, 2 \, n \, \kappa \, \left[(t_m^{(1)})^2 + (t_m^{(2)})^2 \right]^{n-1} \, \left(\boldsymbol{M}^{(1)} \otimes \boldsymbol{N} \otimes \boldsymbol{M}^{(1)} + \boldsymbol{M}^{(2)} \otimes \boldsymbol{N} \otimes \boldsymbol{M}^{(2)} \right) \\ & + 4 \, \kappa \, n \, (n-1) \, \left[(t_m^{(1)})^2 + (t_m^{(2)})^2 \right]^{n-2} \, \left(t_m^{(1)} \, \boldsymbol{M}^{(1)} + t_m^{(2)} \, \boldsymbol{M}^{(2)} \right) \\ & \otimes \left(\boldsymbol{N} \otimes \boldsymbol{M}^{(1)} + \boldsymbol{N} \otimes \boldsymbol{M}^{(2)} \right) , \end{aligned} \tag{81}$$

the linearization is given by

$$\mathrm{d} \llbracket \dot{\boldsymbol{u}} \rrbracket = \mathrm{d}\lambda \, \partial_{\boldsymbol{t}} \phi + \lambda \, \partial^2_{\boldsymbol{t} \otimes \boldsymbol{\sigma}} \phi : \mathrm{d}\boldsymbol{\sigma} . \tag{82}$$

APPENDIX C

This appendix contains the two-dimensional counterpart of the three-dimensional mixed-mode material model summarized in Appendix B. The plane stress model contained in this appendix is employed in the numerical analyses presented in Sections 5-7.

Restricting our considerations to the two-dimensional space, a local CARTESIAN coordinate system at $\boldsymbol{X}_0 \in \partial_{\mathrm{s}} \Omega$ is introduced by means of

$$\boldsymbol{N}, \boldsymbol{M} \in \mathbb{R}^2, \quad ||\boldsymbol{N}||_2 = ||\boldsymbol{M}||_2 = 1 \quad \text{and} \quad \det(\boldsymbol{N}|\boldsymbol{M}) = 1. \tag{83}$$

With Equations (83), the components of the traction vector $\boldsymbol{t} = \boldsymbol{\sigma} \cdot \boldsymbol{N}$ are computed as

$$t_n := (\boldsymbol{N} \otimes \boldsymbol{N}) : \boldsymbol{\sigma} \quad \text{and} \quad t_m := (\boldsymbol{N} \otimes \boldsymbol{M}) : \boldsymbol{\sigma} . \tag{84}$$

Rewriting of the yield function (77) into a two-dimensional context, setting $n = 2$ and assuming $\kappa = \text{const}$, leads to the space of admissible stresses

$$\mathbb{E}_{\boldsymbol{t}} = \{ (\boldsymbol{t}, q) \in \mathbb{R}^3 \times \mathbb{R}_+ \mid \phi(\boldsymbol{t}, q) \leq 0 \} \quad \text{with} \quad \phi(\boldsymbol{t}, q) = \boldsymbol{t} \cdot \boldsymbol{N} + \kappa \, (\boldsymbol{t} \cdot \boldsymbol{M})^2 - q(\alpha) . \tag{85}$$

The mixed-mode material model is completed by the evolution equations. Analogously to Appendix B, these equations are derived using the principle of maximum dissipation. The resulting associative model is summarized in Table 1.

1. yield function:

$$\phi(\boldsymbol{\sigma}, q(\alpha)) = (\boldsymbol{N} \otimes \boldsymbol{N}) : \boldsymbol{\sigma} + \kappa \ [(\boldsymbol{N} \otimes \boldsymbol{M}) : \boldsymbol{\sigma}]^2 - q(\alpha) \tag{86}$$

2. associative flow rule:

$$[\![\dot{\boldsymbol{u}}]\!] = \lambda \ \partial_{\boldsymbol{t}} \phi = \lambda \ [\boldsymbol{N} + 2 \ \kappa \ \boldsymbol{\sigma} : (\boldsymbol{N} \otimes \boldsymbol{M}) \ \ \boldsymbol{M}] \tag{87}$$

3. associative hardening/softening law:

$$\dot{q} = \partial_\alpha q \ \dot{\alpha} =: -H \ \dot{\alpha} \quad \text{with:} \quad \dot{\alpha} = \lambda = [\![\dot{\boldsymbol{u}}]\!] \cdot \boldsymbol{N} =: [\![\dot{\boldsymbol{u}}]\!]_n \tag{88}$$

4. linearization of $[\![\dot{\boldsymbol{u}}]\!]$

$$\mathrm{d}\,[\![\dot{\boldsymbol{u}}]\!] = \mathrm{d}\lambda \ \partial_{\boldsymbol{t}} \phi + \lambda \ \partial_{\boldsymbol{t} \otimes \boldsymbol{\sigma}} \phi : \mathrm{d}\boldsymbol{\sigma} \tag{89}$$

with

$$\partial^2_{\boldsymbol{t} \otimes \boldsymbol{\sigma}} \phi = 2 \ \kappa \ \boldsymbol{M} \otimes \boldsymbol{N} \otimes \boldsymbol{M} \tag{90}$$

Table 1: Two-dimensional mixed-mode material model.

References

[1] J. Hadamard. Leçons sur la Propagation des Ondes. *Librairie Scientifique A. Hermann et Fils, Paris*, 1903.

[2] J.E. Marsden and T.J.R. Hughes. *Mathematical foundation of elasticity*. Dover, New York, 1994.

[3] R. De Borst. *Non-linear analysis of frictional materials*. PhD thesis, Technical University Delft, 1986.

[4] R. De Borst. Some recent issues in computational mechanics. *International Journal for Numerical Methods in Engineering*, 52:63–95, 2001.

[5] G. Pijaudier-Cabot and Z.P. Bažant. Nonlocal damage theory. *Journal of Engineering Mechanics (ASCE)*, 113:1512–1533, 1987.

[6] Z.P. Bažant and G. Pijaudier-Cabot. Nonlocal damage, localization, instability and convergence. *Journal of Applied Mechanics*, 55:287–293, 1988.

[7] H.B. Mühlhaus and E.C. Aifantis. A variational principle for gradient plasticity. *International Journal for Solids and Structures*, 28:845–857, 1991.

[8] R. De Borst and H.B. Mühlhaus. Gradient-dependent plasticity: Formulation and algorithmic aspects. *International Journal for Numerical Methods in Engineering*, 35:521–539, 1992.

[9] R. De Borst. Simulation of strain localization: A reappraisal of the cosserat continuum. *Engineering Computations*, 8:317–332, 1991.

[10] P. Steinmann and K.J. Willam. Localization within the framework of micropolar elastoplasticity. In V. Mannl, J. Najar, and O. Brüller, editors, *Advances in continuum mechanics*, pages 296–313. Springer, Berlin-Heidelberg, 1991.

[11] E.N. Dvorkin, A. M. Cuitiño, and G. Gioia. Finite elements with displacement interpolated embedded localization lines insensitive to mesh size and distortions. *International Journal for Numerical Methods in Engineering*, 30:541–564, 1990.

[12] M. Klisinski, K. Runesson, and S.. Sture. Finite element with inner softening band. *Journal of Engineering Mechanics (ASCE)*, 117(3):575–587, 1991.

[13] J. Simo, J. Oliver, and F. Armero. An analysis of strong discontinuities induced by strain softening in rate-independent inelastic solids. *Computational Mechanics*, 12:277–296, 1993.

[14] J. Oliver. Modelling strong discontinuities in solid mechanics via strain softening constitutive equations part 1: Fundamentals. part 2: Numerical simulations. *International Journal for Numerical Methods in Engineering*, 39:3575–3623, 1996.

[15] F. Armero. Large-scale modeling of localized dissipative mechanisms in a local continuum: applications to the numerical simulation of strain localization in rate-dependent inelastic solids. *Mechanics of Cohesive-Frictional Materials*, 4:101–131, 1999.

[16] J. Mosler and G. Meschke. 3D modeling of strong discontinuities in elastoplastic solids: Fixed and rotating localization formulations. *International Journal for Numerical Methods in Engineering*, 57:1553–1576, 2003.

[17] N. Moës, J. Dolbow, and T. Belytschko. A finite element method for crack growth without remeshing. *International Journal for Numerical Methods in Engineering*, 46:131–150, 1999.

[18] G.N. Wells and L.J. Sluys. A new method for modelling cohesive cracks using finite elements. *International Journal for Numerical Methods in Engineering*, 50:2667–2682, 2001.

[19] M. Jirásek and T. Zimmermann. Embedded crack model: Part I: Basic formulation, Part II: Combination with smeared cracks. *International Journal for Numerical Methods in Engineering*, 50:1269–1305, 2001.

[20] F. Armero. Localized anisotropic damage of brittle materials. In D.R.J. Owen, E. Oñate, and E. Hinton, editors, *Computational Plasticity*, volume 1, pages 635–640, 1997.

[21] J. Mosler and O.T. Bruhns. A 3D anisotropic elastoplastic-damage model using discontinuous displacement fields. *International Journal for Numerical Methods in Engineering*, 60:923–948, 2004.

[22] J. Simo and J. Oliver. A new approach to the analysis and simulation of strain softening in solids. In Z.P. Bažant, Z. Bittnar, M. Jirásek, and J. Mazars, editors, *Fracture and Damage in Quasibrittle Structures*, pages 25–39. E. &F.N. Spon, London, 1994.

[23] F. Armero and K. Garikipati. An analysis of strong discontinuities in multiplicative finite strain plasticity and their relation with the numerical simulation of strain localization in solids. *International Journal for Solids and Structures*, 33:2863–2885, 1996.

[24] A.R. Regueiro and R.I. Borja. Plane strain finite element analysis of pressure sensitive plasticity with strong discontinuity. *International Journal for Solids and Structures*, 38:3647–3672, 2001.

[25] N. Sukumar, N. Moës, B. Moran, and T. Belytschko. Extended finite element method for three-dimensional crack modelling. *International Journal for Numerical Methods in Engineering*, 48:1549–1570, 2000.

[26] J. Oliver. Continuum modelling of strong discontinuities in solid mechanics. In D.R.J. Owen, E Oñate, and E. Hinton, editors, *Proc., 4th Int. Conf. Computational Plasticity*, volume 1, pages 455–479, 1995.

[27] G.N. Wells, L.J. Sluys, and R. De Borst. Simulating the propagation of displacement discontinuities in a regularised strain-softening medium. *International Journal for Numerical Methods in Engineering*, 53:1235–1256, 2002.

[28] J. Oliver and J. Simo. Modelling strong discontinuities in solid mechanics by means of strain softening constitutive equations. In H. Mang, N. Bićanić, and R. de Borst, editors, *Computational Modelling of concrete structures*, pages 363–372. Pineridge press, 1994.

[29] J. Oliver. Continuum modelling of strong discontinuities in solid mechanics using damage models. *Computational Mechanics*, 17(1-2):49–61, 12 1995.

[30] J. Mosler. *Finite Elemente mit sprungstetigen Abbildungen des Verschiebungsfeldes für numerische Analysen lokalisierter Versagenszustände in Tragwerken*. PhD thesis, Ruhr Universität Bochum, 2002.

[31] I. Stakgold. *Green's functions and boundary value problems*. Wiley, 1998.

[32] J.C. Simo and S. Rifai. A class mixed assumed strain methods and the method of incompatible modes. *International Journal for Numerical Methods in Engineering*, 29:1595–1638, 1990.

[33] J.C. Simo and F. Armero. Geometrically non-linear enhanced strain mixed methods and the method of incompatible modes. *International Journal for Numerical Methods in Engineering*, 33:1413–1449, 1992.

[34] C. Miehe and J. Schröder. Post-critical discontinuous analysis of small-strain softening elastoplastic solids. *Archive of Applied Mechanics*, 64:267–285, 1994.

[35] J. Simo and T.J.R. Hughes. *Computational inelasticity*. Springer, New York, 1998.

[36] U. Ohlsson and T. Olofsson. Mixed-mode fracture and anchor bolts in concrete: Analysis with inner softening bands. *Journal of Engineering Mechanics (ASCE)*, 123:1027–1033, 1997.

[37] J. Mosler. Numerical analyses of discontinuous material bifurcation: Strong and weak discontinuities. *Computer Methods in Applied Mechanics and Engineering*, 2004. in press.

[38] C. Geiger and C. Kanzow. *Theorie und Numerik restringierter Optimierungsaufgaben*. Springer, 2002.

[39] R.I. Borja. A finite element model for strain localization analysis of strongly discontinuous fields based on standard galerkin approximation. *Computer Methods in Applied Mechanics and Engineering*, 190:1529–1549, 2000.

[40] J. Mosler and G. Meschke. FE-modeling of displacement discontinuities in inelastic continua. *Zeitschrift für Angewandte Mathematik und Mechanik*, 81(Suppl. 4):875–876, 2001.

[41] J. Mosler and G. Meschke. Analysis of mode I failure in brittle materials using the strong discontinuity approach with higher order elements. In *2. European Congress on Computational Mechanics*, 2001.

[42] J. Mosler. On the efficient implementation of an elastoplastic damage model for large-scale analyses of material failure: A multiscale approach. *Computers & Structures*, 2004. accepted.

[43] J. Mosler. A novel algorithmic framework for the numerical implementation of locally embedded strong discontinuities. *Computational Mechanics*, 2004. submitted.

[44] P. Dumstorff, J. Mosler, and G. Meschke. Advanced discretisation methods for cracked structures: The strong discontinuity approach vs. the extended finite element method. In E. Onate D.R.J. Owen and B. Suaŕez, editors, *Computational Plasticity VII*, page p. 89. CIMNE, COMPLAS 2003: 07.-10.04.2003 in Barcelona 2003. CD-ROM.

[45] J. Schröder and Löblein. J. Computational aspects of crack-simulations using triangular elements with embedded interfaces. In F. Stangenberg, O.T. Bruhns, D. Hartmann, and G. Meschke, editors, *2nd International Conference Lifetime-Oriented Design Concepts*, pages 157–166. SFB 398, Ruhr-Universität Bochum, 2004.

[46] G. Bolzon and A. Corigliano. Finite elements with embedded displacement discontinuity: a generalized variable formulation. *International Journal for Numerical Methods in Engineering*, 49:1227–1266, 2000.

[47] R. Tano, M. Klisinski, and Th. Olofsson. Stress locking in the inner softening band method: A study of the origin and how to reduce the effects. In R. de Borst, N. Bićanić, H. Mang, and G. Meschke, editors, *Computational Modelling of Concrete Structures, EURO C-98*, volume 1, pages 329–335, 1998.

[48] M. Schmidt-Baldassari. Numerical concepts for rate-independent single crystal plasticity. *Computer Methods in Applied Mechanics and Engineering*, 192:1261–1280, 2003.